

REPORT DOCUMENTATION PAGE

AFRL-SR-BL-TR-00-

Public reporting burden for this collection of information is estimated to average 1 hour per response, in gathering and maintaining the data needed, and completing and reviewing the collection of information. collection of information, including suggestions for reducing this burden, to Washington Headquarters S Davis Highway, Suite 1204, Arlington, VA 22202-4302, and to the Office of Management and Budget,

sources,
ct of this
Jefferson
i.

1. AGENCY USE ONLY (Leave blank)	2. REPORT DATE	3. REPORT NUMBER	1 Aug 96 - 31 Dec 99
4. TITLE AND SUBTITLE		5. FUNDING NUMBERS	
Unified Retrieval of Cloud Properties, Atmospheric Profiles, and Surface Parameters from Combined DMSP Imager and Sounder Data		F49620-96-C- 0025	
6. AUTHOR(S)			
R.G. Isaacs			
7. PERFORMING ORGANIZATION NAME(S) AND ADDRESS(ES)		8. PERFORMING ORGANIZATION REPORT NUMBER	
Atmospheric and Environmental Research, Inc. 840 Memorial Drive Cambridge, MA 02139-377			
9. SPONSORING/MONITORING AGENCY NAME(S) AND ADDRESS(ES)		10. SPONSORING/MONITORING AGENCY REPORT NUMBER	
AFOSR 801 North Randolph Street, Room 732 Arlington, VA 22203-1977		F49620-96-C-0025	
11. SUPPLEMENTARY NOTES			
12a. DISTRIBUTION AVAILABILITY STATEMENT		12b. DISTRIBUTION CODE	
Approved for public release, distribution unlimited			
13. ABSTRACT (Maximum 200 words)			
The main objective of the proposed study was to investigate the complementary information provided by microwave and infrared sensors in order to enhance both the microwave retrieval and the current cloud analysis. This primary task investigated and assessed the impact of incorporating cloud horizontal and vertical spatial distribution information on the performance and accuracy of simultaneous physical retrievals of atmospheric profiles from microwave sensors. The second task explored additional attributes of the microwave measurements, particularly related to ice clouds, to investigate the possibility of identifying multi-layer clouds from simultaneous microwave, visible and infrared data, and to provide infrared emission properties needed for threshold-based cloud detection. We also applied the UR approach to DMSP data to provide the basis for screening out cases where the infrared/visible-derived low cloud properties were uncertain and to assess ability to characterize the vertical structure of multi-layer clouds. The third task investigated the feasibility of predicting infrared emission properties using the microwave data, and assessed if this information could be used to enhance low cloud and thin high cloud identification in totally overcast conditions, especially at night. This task included deriving empirical relationships between microwave and infrared surface emission based on dependent clear data sets, and performing exploratory cloud analyses using both the surface temperature data from the current surface temperature data base and the microwave derived surface emission properties. The last task addressed the application of the UR algorithm to land and to snow/ice backgrounds and assessed the algorithm's capability using new data collected over the Northern Hemisphere in the winter.			
14. SUBJECT TERMS		15. NUMBER OF PAGES	
Multisensor, cloud analysis; ice cloud properties; Unified Retrieval technique; DMSP; land infrared emission properties; microwave emission properties; snow and ice backgrounds.		59	
		16. PRICE CODE	
17. SECURITY CLASSIFICATION OF REPORT	18. SECURITY CLASSIFICATION OF THIS PAGE	19. SECURITY CLASSIFICATION OF ABSTRACT	20. LIMITATION OF ABSTRACT



**Atmospheric and
Environmental Research, Inc.**

**Unified Retrieval of Cloud Properties, Atmospheric
Profiles, and Surface Parameters from Combined
DMSP Imager and Sounder Data**

Final Report

1 August 1996 - 31 December 1999

PIIN F49620-96-C-0025

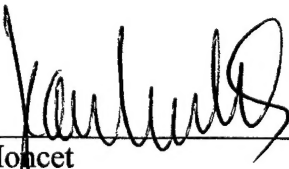
Submitted by:

Sid Boukabara, Jennifer Hegarty, Chris Lietzke, Richard Lynch,
Jean-Luc Moncet, and Ronald G. Isaacs
Atmospheric and Environmental Research, Inc.
840 Memorial Drive
Cambridge, MA 02139

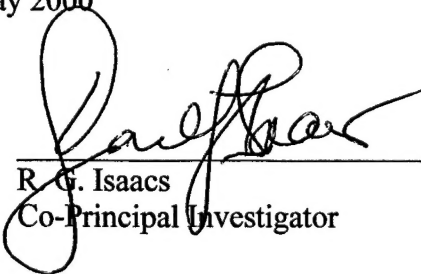
Submitted to:

Paul J. Bellaire Jr., Colonel, USAF
Program Manager, Atmospheric Sciences
Air Force Office of Scientific Research
110 Duncan Avenue, Suite B115
Bolling AFB, DC 20332-8050

1 May 2000



J.-L. Moncet
Co-Principal Investigator



R. G. Isaacs
Co-Principal Investigator

20000817 103

INTRODUCTION	5
FORWARD MODELING IMPROVEMENTS FOR MICROWAVE AND INFRARED RADIATIVE TRANSFER.....	10
IMPACT OF CLOUD MODELING ERRORS ON MICROWAVE RETRIEVAL PERFORMANCE...	11
CLOUD COVER PREDICTION USING MICROWAVE AND INFRARED OBSERVATIONS.....	14
IDENTIFICATION OF ICE CLOUDS.....	18
IDENTIFICATION OF MULTI-PHASE WATER CLOUDS.....	22
RETRIEVALS OVER LAND SURFACES.....	24
EMISSIVITY BACKGROUND TIME AVERAGING EXPERIMENTS.....	24
SURFACE AIR TEMPERATURE RETRIEVAL USING SSM/I	34
TEMPERATURE PROFILE RETRIEVAL OVER LAND/SNOW/ICE USING AMSU	35
CONCLUSIONS	44
REFERENCES.....	45

The research described in this report further explores the application of the Unified Retrieval (UR) approach developed by Isaacs and Moncet (Isaacs, 1989; Moncet et al., 1996). The objectives of this research effort are designed to bring the UR approach closer to operational implementation using DMSP sensors. The tasks from the statement of work are outlined below.

Task 1 – Enhancement of Unified Retrieval with Implementation of Multi-sensor Cloud Analysis Algorithms

The main objective of the proposed study is to investigate the complementary information provided by microwave and infrared sensors in order to enhance both the microwave retrieval and the current cloud analysis. This task will investigate and assess the impact of incorporating cloud horizontal and vertical spatial distribution information on the performance and accuracy of simultaneous physical retrievals of atmospheric profiles from microwave sensors.

Task 2 - Retrieval of Ice Cloud Properties

Explore additional attributes of the microwave measurements, particularly related to ice clouds, to investigate the possibility of identifying multi-layer clouds from simultaneous microwave, visible and infrared data, and to provide infrared emission properties needed for threshold-based cloud detection. We will also apply the UR approach to DMSP data to provide the basis for screening out cases where the infrared/visible derived low cloud properties are uncertain and to assess ability to characterize the vertical structure of multi-layer clouds.

Task 3 - Predicting Infrared Emission Properties over Land Using Microwave Data

Investigate the feasibility of predicting infrared emission properties using the microwave data. Assess if this information could be used to enhance low cloud and thin high cloud identification in totally overcast conditions especially at night. This task will include deriving empirical relationships between microwave and infrared surface emission based on dependent clear data sets, and performing exploratory cloud analyses using both the surface temperature data from the current surface temperature data base and the microwave derived surface emission properties.

Task 4 - Retrievals over Land - Snow and Ice Backgrounds

Address the application of the UR algorithm to land and to snow/ice backgrounds. This task will assess the algorithm's capability using new data collected over the Northern Hemisphere in the winter.

Introduction

Current atmospheric remote sensing systems are limited primarily by the available hardware technology. Operational IR satellite sounders use broadband radiometers supplemented by microwave sounders in cloudy regions with only a limited number of channels. As technology evolves and with the prospect of future advanced technology high spectral resolution sounders such as AIRS or the EUMETSAT Interferometer Thermal Sounder (ITS), it is likely that a greater emphasis will be put on the processing algorithms. In particular, the accuracy achievable with any system depends in large part on the ability to separate the contributions of cloud/aerosols and surface properties from that of the atmosphere, the largest natural sources of "noise" for atmospheric temperature and moisture retrievals. Sounding (atmospheric profiles) and imaging (cloud, surface properties) parameters are traditionally treated separately using analysis methods that are fundamentally different. While physical algorithms that attempt to model the physics of atmospheric radiation are commonly employed for extracting temperature and water vapor profiles from infrared measurements, classification type methods are the most popular approach for clouds and surface properties, both in the microwave and infrared/visible. Even for soundings, the microwave community relies heavily on regression type approaches to process the sounding information. The consequences are a limited capability to properly treat cloud and surface emissivity effects and a domain of application for many parameters effectively limited to benign ocean surface backgrounds.

In light of these considerations, it is anticipated that a combination of sounding and imaging functions is potentially quite useful. For instance, cloud properties can be used to correct the sounding information and similarly sounding information can be used in the cloud

analysis to provide better estimates of cloud layers and cloud top height. Similar benefits may be expected by offering a consistent treatment of the surface emissivity. Fidelity in surface emissivity retrievals potentially provides more accurate retrieval of near surface temperature and moisture and CLW. It also insures better depiction of the spatial distribution of these near surface meteorological fields against backgrounds with spatially variable radiometric properties. Finally, the surface emissivity retrievals themselves contain a wealth of information on precisely those surface properties (surface type, vegetation, soil moisture, snow and ice properties, etc.) sought by imaging algorithms with the added advantage that atmospheric "effects" have been accounted for within the context of the overall retrieval process.

To accomplish unification of the sounding and imaging retrieval functions as described above, requires that the formalism used for the inversion be flexible enough to treat information from different sensor types, i.e. sounders and imagers. The Unified Retrieval (UR) algorithm described here is a general nonlinear physical retrieval algorithm for the simultaneous retrieval of temperature profiles, water vapor profiles, cloud properties and, surface temperature and emissivity from multi-sensor platforms. At this stage of development, the UR algorithm makes use of the microwave sounding and imaging sensor data that are the primary meteorological sensors aboard the DMSP 5D-2 spacecraft. In overcast situations, microwave sensors become the primary source of information, i.e. the retrieval performance in these cases is controlled by the microwave algorithm. Although the concept is demonstrated for the current DMSP microwave sensor suite as well as AMSU-A, the domain of applicability of the algorithm includes DMSP 5D-3 (OLS-SSMIS) and infrared/microwave sounder suites (such as HIRS/AMSU aboard the TIROS KLM spacecraft). It is also applicable to potential future sensors suites aboard NPOESS platforms.

Use of electro-optical (EO) (i.e. infrared and visible) cloud imager data from GOES-8 sounder is used as well within the present scheme. In general, the primary use of the imaging data is in the characterization of the distribution of CLW within the field-of-view of the microwave sensors and determination of surface temperatures. As it will be discussed later, for large cloud amounts, radiances depend significantly on fractional cloud cover and cloud top height. The difficulty in combining the microwave and infrared/visible information is that the latter are sensitive to ice clouds that are mostly transparent to the microwave radiation. Therefore, one must carefully treat the two types of clouds in the determination of the spatial distribution. Another factor that must be considered in merging the two sources of information is that cloud analysis greatly benefits from the knowledge of atmospheric profiles of moisture and temperature as determined from the microwave measurements. This information helps not only in specifying a cloud top altitude but also provides for more accurate detection of clouds.

The UR algorithm is a point-by-point retrieval method, i.e. it is assumed that all channels have the same footprint on the ground. To accommodate this approach, the imaging information is simply averaged over the larger footprint of the sounding channels. The rationale for adopting this kind of approach is the simplicity of implementation and the fact that we are mostly interested, at this stage, in the spectral information content of the available measurements. Note that the point-by-point approach is non-optimal in the sense that it does not take full advantage of the spatial information content available from the DMSP or the GOES channels. Also, problems may arise with such a method for parameters that have highly nonlinear effects on the observed radiances such as clouds. In this case, the algorithm may not converge if the spatial distribution of clouds is not adequately specified, for example, using cloud imager data.

One aspect of the DMSP sensor configuration that must be taken into consideration in the context of the proposed algorithm is the mixed scan mode of the DMSP sounder and imager combination. While the sounding channels are cross-track scanning, the SSM/I sensor uses a conical scanning mode with fixed earth local incidence angle of 53°. The conical scanning mode of the SSM/I maintains footprint size and polarization integrity throughout the scan, an important feature for the imaging functions of the sensor. The different paths viewed by the sounder and imager and the approximately 4 minute time lag between collocated measurements may cause difficulties in highly inhomogeneous situations and prevent the simultaneous processing of the two sources of information with simple point-by-point methods. In most cases, however, it appears that the gain obtained by exploiting the synergy between sounding and imaging information exceeds the potential negative impact of the differences in the scan mode of the two sensors. In conditions of extreme inhomogeneity, as indicated for instance by the spatial variance of the higher frequency imaging channels exceeding some threshold value, it is always possible to ignore part of the imaging information.

The method used for the inversion of the satellite-measured radiances is the standard maximum likelihood method described by Rodgers (1976). This method belongs to a class of constrained least-squares approaches that finds an estimate \hat{x} of the state vector by minimizing a cost function of the form:

$$J(x) = (y^m - y(x))^T W (y^m - y(x)) + (x - x_0)^T \Gamma (x - x_0), \quad (1)$$

where, y^m is the vector of observed satellite sensor channel radiometric measurements, $y(x)$

are the calculated radiances which are related to the desired atmospheric/surface parameter state vector \mathbf{x} through the radiative transfer or forward problem model, \mathbf{x}_0 is a supplied independent estimate of the state vector (sometimes called the "first-guess"), and W and Γ are some appropriate weighting matrices.

The maximum likelihood approach relies on the existence of an *a priori* estimate with Gaussian error statistics to produce a solution that is statistically optimal. Given knowledge of the error covariance matrices of the background estimate and the radiometric measurements, S_x and S_ϵ , respectively, the maximum likelihood solution is obtained by taking $W = S_\epsilon^{-1}$ and $\Gamma = S_x^{-1}$ in the previous expression for the cost function. Under these conditions, it can be shown that the solution obtained by minimizing (1) also maximizes the conditional probability of \mathbf{x} given \mathbf{y}^m . This is the solution used by Eyre (1989). Note that the stability of the maximum likelihood solution is controlled by the covariance of the errors in the different elements of the background vector. In that sense, the most appropriate source of *a priori* information is not necessarily one that is close, in an RMS sense, to the true state.

The nonlinear optimization problem described above is solved using the Gauss-Newton iterative procedure. In this case, the background vector is also used as first-guess to start the search procedure. At each iteration step, a new solution is obtained by linearizing the forward model around the previous guess profile and by finding the new state for which the gradient of the cost function vanishes. The solution is updated from \mathbf{x}_n to \mathbf{x}_{n+1} using the following relaxation criteria,

$$\mathbf{x}_{n+1} = \mathbf{x}_n + S_x K_n^T (K_n S_x K_n^T + S_\epsilon)^{-1} [\mathbf{y}^m - \mathbf{y}_n + K_n (\mathbf{x}_n - \mathbf{x}_0)] , \quad (2)$$

where $K_n = \partial y_n / \partial x_n$ is the gradient of the forward model. The gradient values are computed analytically as shown in the Appendix. The iteration process is stopped if one of the convergence criteria is met, such that $y^m - y_n$ is within the radiance noise value or $x_{n+1} - x_n$ is less than some preset threshold.

Forward Modeling Improvements for Microwave and Infrared Radiative Transfer

One of the most critical modules for a physical inversion algorithm is the radiative transfer (RT) model (or forward model). The RT model is used to accurately compute the radiances corresponding to a given atmospheric state and the derivatives (or Jacobian) of the radiances with respect to atmospheric and surface parameters for use by the inversion module. In addition to providing for an accurate treatment of the atmosphere, the forward model must often meet stringent requirements for computation time. The forward model for the UR has been improved to better simulate top of the atmosphere radiances for remote sensing applications. The newly developed Optimal Spectral Sampling (OSS) technique is applied in order to construct a highly accurate, computationally efficient, monochromatic forward model. The previously used model (Eyre and Woolf, 1988), parameterized the atmospheric transmittance profiles, whereas the current model uses interpolated, weighted optical depths to characterize electromagnetic absorption in the atmosphere. Because the OSS technique is a monochromatic method, it has an advantage over other forms of fast-model parameterizations in that it provides the required derivatives with little extra computation time. The OSS model and its application to Microwave and Infrared radiative transfer are described in the Appendix.

Impact of cloud modeling errors on microwave retrieval performance

The forward model used in the Unified Retrieval (UR) assumes a homogeneous horizontal distribution of cloud liquid water in the scene being viewed. An inhomogeneous distribution can cause modeling errors that increase retrieval error. A preliminary assessment of the impact on the retrieval performance is performed for a microwave sensor suite similar to the DMSP 5D2.

The forward model considers radiation in two paths, the upwelling or direct path radiation and the down-welling or indirect path radiation that is specularly reflected into the upwelling path. If a cloud fills different percentages of each path, its radiative impact on the top of the atmosphere radiance may be different. Figure 1 shows the possible scenarios when cloud water is present in each path. The current forward model assumes that one cloud liquid water amount is equally applied in both the upwelling and down-welling paths.

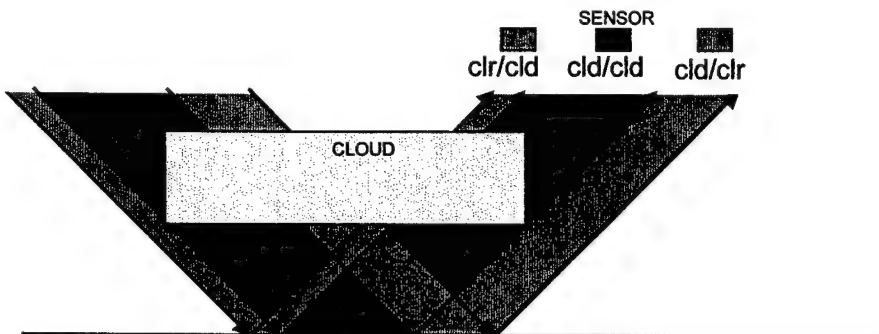


Figure 1. Schematic diagram of a cloud in the down-welling (indirect) and upwelling (direct) paths.

The impact on the simulated brightness temperatures at 183 +/- 3 GHz and 183 +/- 7 GHz by a cloud with liquid water path of 0.01 mm and various cloud top pressures in the

direct, indirect, and both paths is shown in Table 1. These simulations assume 100 % cloud cover in each of the designated paths, however the brightness temperatures can be simulated for any cloud configuration as a linear combination of the impacts in each of the paths scaled by the fractional cloud cover in that path. The retrieval model assumes identical cloud water amount in the upwelling and down-welling paths. This assumption can prevent the inversion algorithm from converging due to an inability to model the cloud sufficiently well. The channels most affected are the low frequency surface viewing channels (e.g. 19 GHz) and the 183 GHz channels.

Table 1. Impact on the simulated brightness temperatures of a 0.01mm cloud with 100 % cloud coverage in indirect, direct and both paths for 2 water vapor sensing channels.

	pressure (mb)	Indirect	Direct	Both
With 183 Ghz \pm 7 GHz	700	0.28	0.12	0.4
	620	0.29	-0.09	0.19
	500	0.32	-0.43	-0.12
With 183 Ghz \pm 3 GHz	700	0.003	-0.04	-0.04
	620	0.0035	-0.16	-0.16
	500	0.004	-0.45	-0.45

The impact on the water vapor profile retrieval performance for a set of ocean profiles and four different cloud amounts is shown in Figure 2. The cloud in all cases had a top of 500 mb and was only in the direct (upwelling) path. The cloud top pressure was assumed known. Figure 2 shows that the water vapor retrieval begins degrade for values of cloud water path in excess of 0.05 mm. The impact on the surface skin temperature (T_{skin}) retrieval for the same experiment is also significant (see Table 2). Land cases were also examined but because of the lower cloud signal over land the impact of cloud modeling errors on the retrieval performance was much less than over the ocean. The results presented here indicate that the impact of cloud modeling errors within the retrieval algorithm can be

significant. This assumption may lead to degraded retrievals in inhomogeneous cloud fields especially near cloud edges.

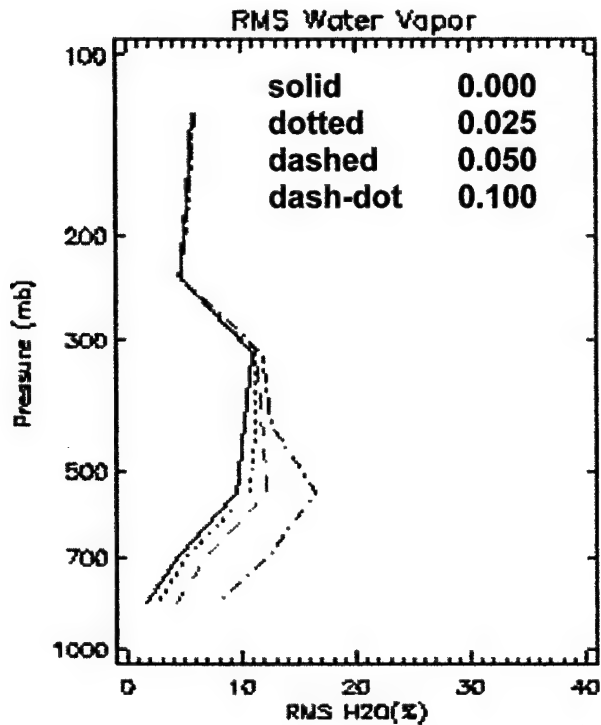


Figure 2. Water vapor profile RMS for a set of ocean profiles and four cloud amounts (mm) in the direct path only. Cloud tops are at 500 mb.

Table 2. Tskin RMS for a set of ocean profiles and four cloud amounts in the direct path only. Cloud tops are at 500 mb.

CLW (mm)	Tskin RMS (K)
0.000	0.65
0.025	0.76
0.050	0.96
0.100	1.52

We are considering several approaches to minimize the impact on the retrieval performance. One approach is to adjust the radiometric error covariance matrix so that the

effective weight of the channels that are impacted most by the presence of cloud inhomogeneities would be reduced. In some situations we might want to eliminate those channels altogether. Another approach is to add a second cloud liquid water amount to the set of retrieved parameters so that there would be an independent amount for both the indirect and direct paths. This would allow for more accurate modeling of the cloud impacts in the forward calculation. Yet, another possibility would be to expand the retrieval process from its current one-dimensional configuration to three dimensions. All of these approaches will be looked at in greater detail in the future.

Cloud cover prediction using microwave and infrared observations

The purpose of this sub-task is to utilize coincident microwave and infrared observations to better identify cloud cover. The method is based on the difference in brightness temperature between the infrared observations and coincident simulated clear sky calculations made using profiles of atmospheric temperature and moisture retrieved from the microwave observations at coincident locations in space and time. First, a swath of DMSP microwave observations are used to simultaneously retrieve the temperature and moisture profiles at each SSM/T-2 pixel (~50 km at NADIR). These profiles are then used to calculate an infrared clear-sky radiance at each of the eighteen GOES-8 sounder frequencies (see Table 3). The differences between these simulated clear-sky brightness temperatures and the observed brightness temperatures are histogrammed to find the scene maximum for each channel which is then subtracted from the differences to give a set of adjusted brightness temperature differences. These adjusted differences are then used as predictors for the visible albedo predictand. A neural net was trained using the predictors and predictand for all

eighteen infrared adjusted brightness temperature differences and twelve longwave and midwave differences (short wave excluded). Multiple linear regression was also evaluated, but the neural net was found to be superior in its ability to predict visible albedo. The results (Figure 3) show that the visible albedo is well predicted ($\text{RMS} = 1.5$) from the eighteen adjusted differences and less so when the shortwave is excluded ($\text{RMS} = 2.6$), as would be expected. Setting the clear sky albedo threshold at 3%, we see that the infrared adjusted differences are able to predict cloud cover quite well as shown in Figure 4 and Figure 5. This method should be superior to straight or relative threshold methods since it is based on the adjusted differences in brightness temperature and is therefore dependent only on the microwave retrieval performance.

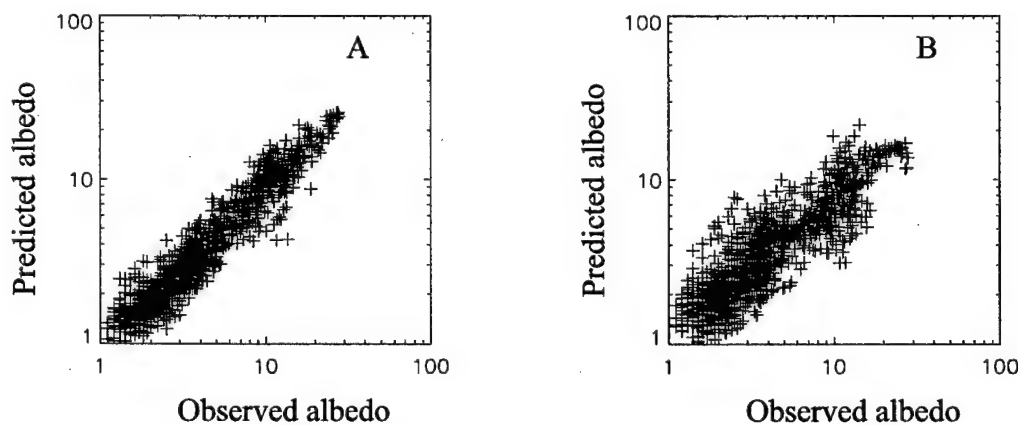


Figure 3. Predicted and observed albedos using adjusted brightness temperature differences for all 18 GOES-8 sounder channels (A) and using 12 longwave and midwave (no short wave) channels (B).

Table 3. Channel characteristics of GOES-8 Sounder (courtesy CIMSS).

Wavelength, μm (Frequency, cm^{-1})	Channel	NedT (K)	Purpose
14.71(680)	1	1.02	Stratosphere temperature
14.37(696)	2	0.87	Tropopause temperature
14.06(711)	3	0.60	Upper-level temperature
13.96(733)	4	0.40	Mid-level temperature
13.37(748)	5	0.45	Low-level temperature
12.66(790)	6	0.20	Precipitable Water
12.02(832)	7	0.13	Surface temp., moisture
11.03(907)	8	0.10	Surface temperature
9.71(1030)	9	0.14	Total ozone
7.43(1345)	10	0.11	Low-level moisture
7.02(1425)	11	0.13	Mid-level moisture
6.51(1535)	12	0.21	Upper-level moisture
4.57(2188)	13	0.13	Low-level temperature
4.52(2210)	14	0.13	Mid-level temperature
4.45(2245)	15	0.16	Upper-level temperature
4.13(2420)	16	0.10	Boundary-layer temperature
3.98(2513)	17	0.17	Surface temperature
3.74(2671)	18	0.10	Surface temp., moisture
0.94(14367)			Cloud

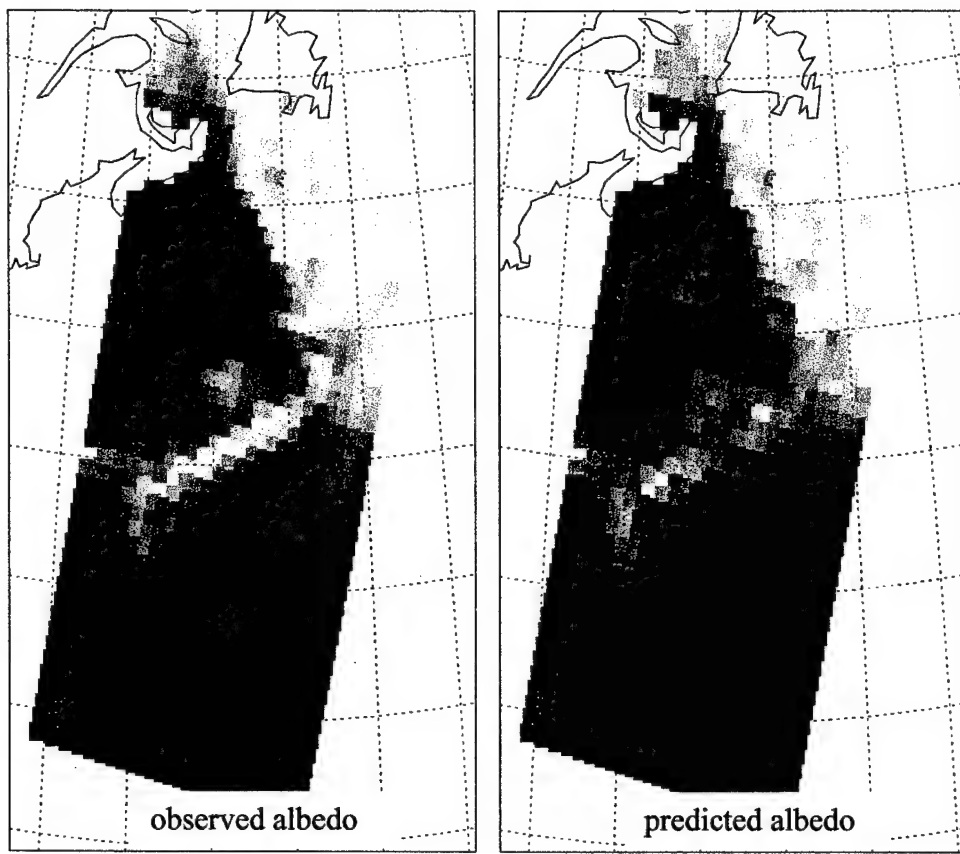


Figure 4. Observed and predicted visible albedos for August 22, 1995 1038Z using all eighteen GOES sounder infrared channels (includes shortwave).

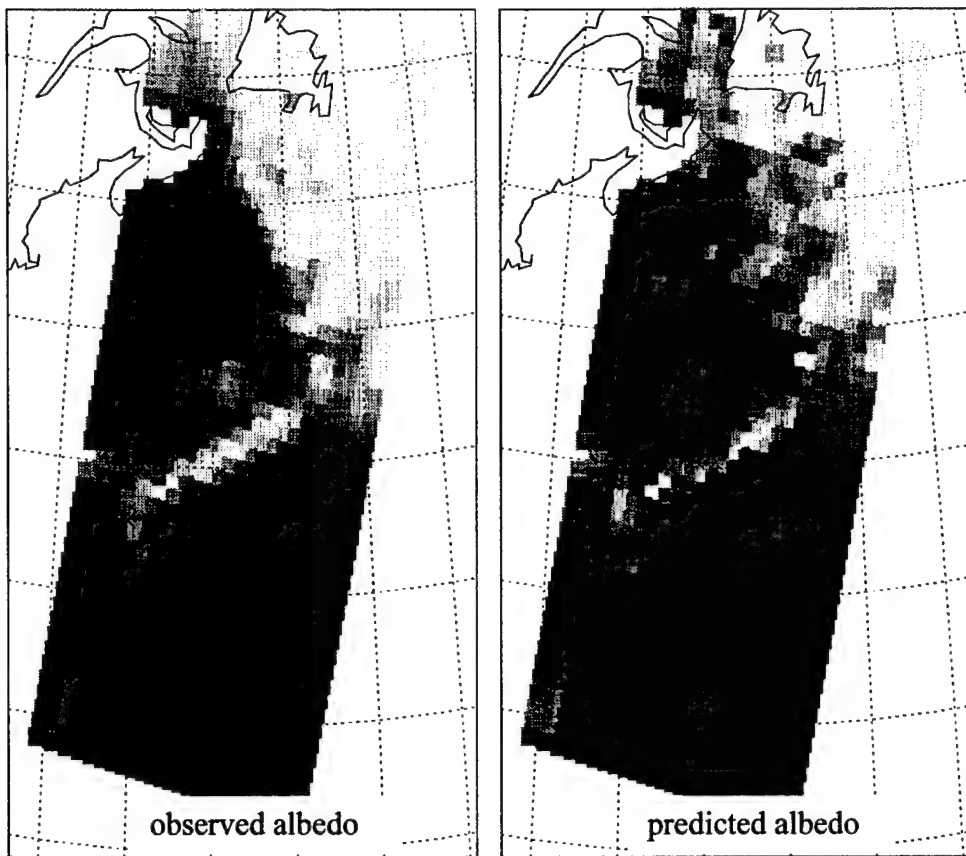


Figure 5. Observed and predicted visible albedos for August 22, 1995 1038Z without shortwave channels.

Identification of ice clouds

Ice clouds can easily be identified by cold brightness temperatures in the window channels (e.g. channels 6, 7, 8 on the GOES sounder) provided that the clouds are optically thick at those frequencies. Since optically thick ice clouds usually occur only in convective regions, many optically thin ice clouds would be classified as low (water) clouds using window channel brightness temperatures alone. However, using a microwave-based retrieval of temperature and moisture in the infrared forward model along with the observed

brightness temperatures, we are able to identify clouds in the sounder channels that are optically thin. The previously mentioned adjusted brightness temperature differences are used to identify the presence of optically thin ice clouds. Thresholds are set on two sounder channels (3, 12) and two window channels (7, 8). If the adjusted brightness temperature difference on the sounder channels exceeds 2 K and the adjusted brightness temperature difference on the window channels exceeds 2 K then there is an ice cloud present. If the adjusted brightness temperature difference on the sounder channels exceeds 2 K and the adjusted brightness temperature difference on the window channels exceeds 2 K and is less than 21 K ($3 \text{ km} * 7 \text{ K/km}$) then there is an optically thin ice cloud present. The value of 21 K is subjective, but is taken to be a value ($3 \text{ km} \sim 700 \text{ mb}$) known to be considerably lower than the maximum of the sounding channels' weighting functions (see Figure 6, Figure 7). The identification of such clouds is shown by the orange shading in the plot (left side) of Figure 8. The window channel brightness temperature of the optically thin cloud area is in the 271 to 276 K range. From the window channels alone, we would be unable to distinguish optically thick low clouds from optically thin high clouds. However, using the MW retrieval along with the sounder channels we are able to do so, thereby providing a better estimation of cloud top height.

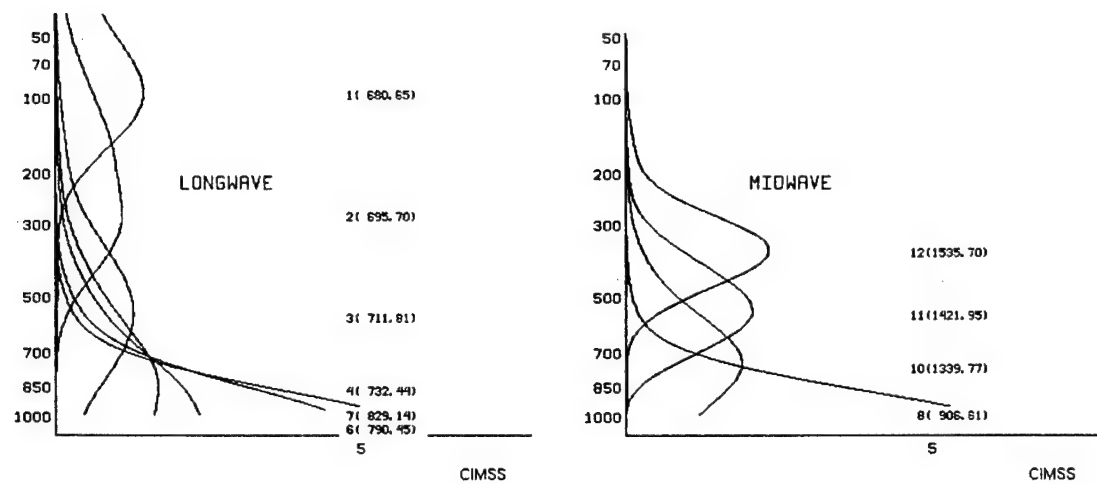


Figure 6. Long wave and mid wave temperature weighting functions for GOES 8 sounder (courtesy CIMSS, <http://cimss.ssec.wisc.edu>).

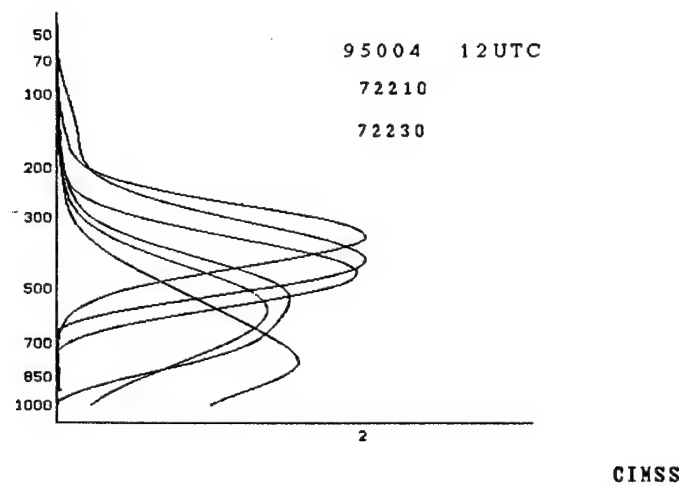


Figure 7. Mid wave water vapor weighting functions for GOES 8 sounder (courtesy CIMSS, <http://cimss.ssec.wisc.edu>).

Tb (K): 211 216 221 226 231 236 241 246 251 256 261 276 281 286 291 296

Optically Thin Clouds in Orange

Channel 8 Brightness Temperature (K)



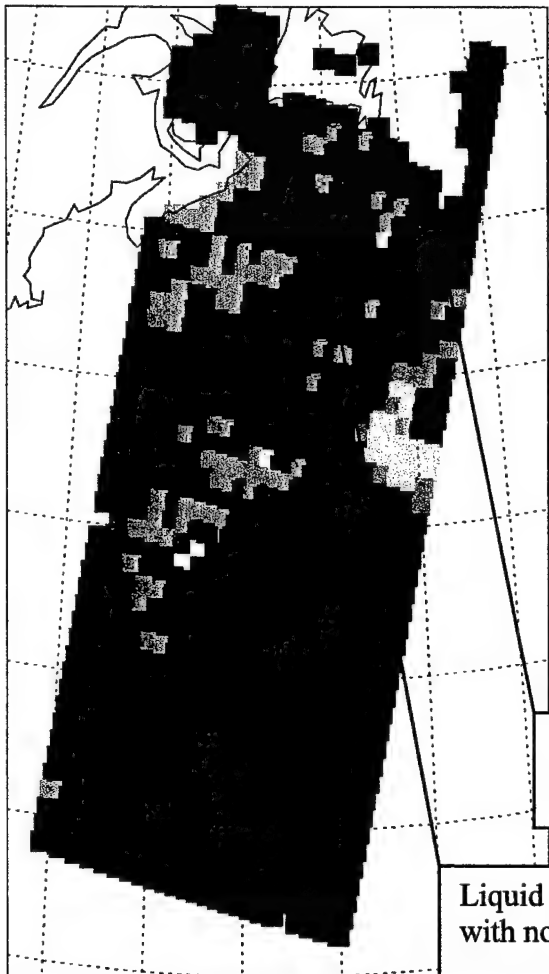
Figure 8. Optically thin cloud identification (left) and channel 8 (window, 907 cm^{-1}) brightness temperatures (right).

Identification of multi-phase water clouds

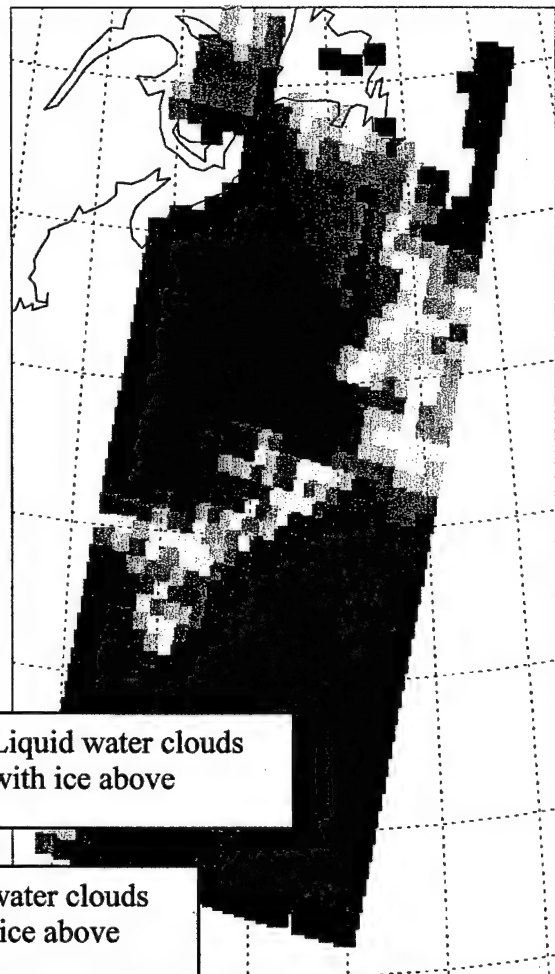
Multi-phase clouds, which may be multi-layered, are found by the coincident identification of ice and liquid present at the same location. The ice clouds may be optically thin or thick, while the MW retrieval produces coincident cloud liquid water retrievals in excess of 0.02 mm. As seen in Figure 9, most of the liquid water in this scene is coincident with optically thick ice or low, liquid phase clouds.

Tb (K): 211 216 221 226 231 236 241 246 251 256 261 276 281 286 291 296

Liquid Water Clouds in Red



Channel 8 Brightness Temperature (K)



Liquid water clouds
with ice above

Liquid water clouds
with no ice above

Figure 9. Multi-phase cloud identification.

Retrievals over Land Surfaces

Since surface emissivity as a function of frequency is retrieved simultaneously with profiles of temperature and moisture, it is necessary to have a statistically representative background mean and covariance for the physical inversion (UR). We have chosen to use emissivities retrieved from SSM/I measurements by Prigent, et al. (1997). This database contains a global representation of the microwave surface emissivity from 19 GHz to 85 GHz during October. Emissivity spectra, randomly selected from this database, are used to construct the background mean and covariance. The retrieval of the frequency dependent, emissivity state vector simultaneously with the other state vector parameters (temperature profile, moisture profile, skin surface temperature, cloud liquid water, and cloud top height) is effectively constrained by the statistics derived from the Prigent data. The Prigent emissivities are interpolated and extrapolated to the AMSU frequencies for the background calculation when appropriate.

Emissivity background time averaging experiments

Using the unified retrieval technique at SSM/I frequencies, we have investigated the effect of using a time sequence of retrieved emissivities to generate a new background and covariance for input into future applications of the UR. In particular, we are exploring the improvements on the retrieved skin temperature that may be realized using time-averaged emissivities. We have a set of either NOAA-88 sonde points or NWP grid points each with an assigned constant emissivity profile. Sixteen independent UR retrievals are executed varying the instrument noise or cloud amount and height or both. The variables retrieved are skin temperature, emissivity profile, TPW, CLW, and some atmospheric temperature profile

information. Considering SSM/I over land is most sensitive to emissivity and skin temperature we focus on these two parameters. With the first sixteen retrievals we generate an average emissivity profile along with a covariance matrix. These are then used in another retrieval as the background and covariance. We first looked at 1176 NOAA-88 atmospheric profiles with an emissivity profile picked from Prigent's data set of monthly mean emissivities. Next, we looked at a set of 176 NWP profiles also with an emissivity profile from Prigent. Figure 10 shows the RMS difference between the input and the average of the retrieved emissivity and the instantaneous retrieved emissivity for the seven channels for the sixteen runs.

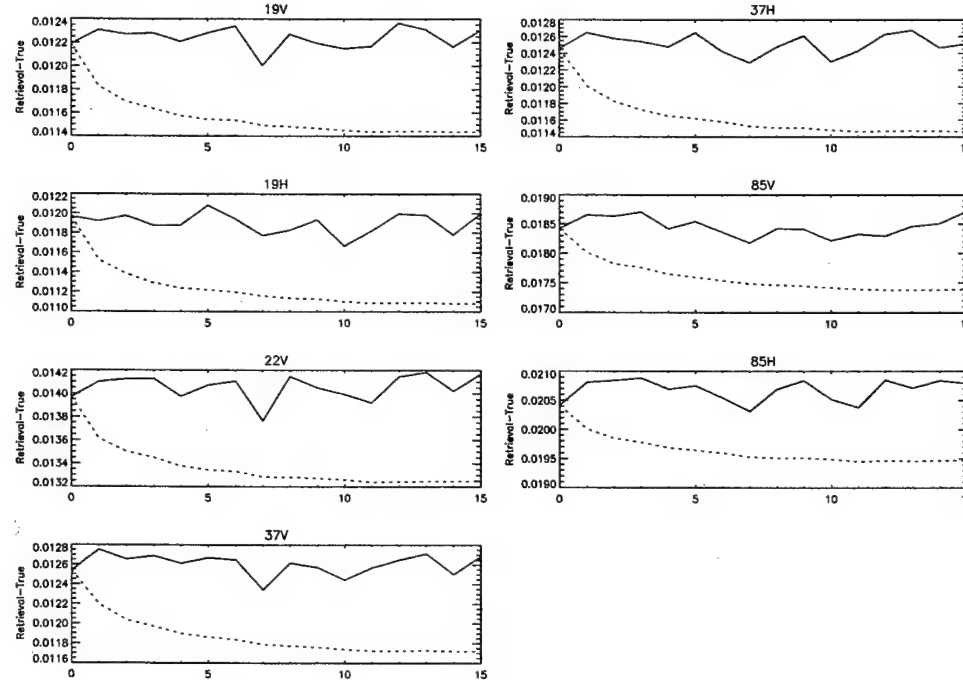


Figure 10. RMS difference between input and averaged (dotted line) and instantaneous (solid line) for all seven channels and sixteen runs. Clear sky conditions with varying noise.

These are for the case of clear sky NOAA-88 profiles only varying instrument noise. The averaged emissivities converge to values that in a root-mean-square sense are closer to

the truth than the retrieved at any one instance. The RMS difference between the converged average and the input is given in column A in Table 4. We perform two more clear sky runs with the same noise. The first is like the previous sixteen, emissivity covariance and background based upon a global data set. The next uses the background mean and covariance based upon the previous sixteen runs. The RMS difference between truth and retrieved for the emissivities are also shown in Table 4. Of course column C is very close to column A since the covariance is now very tight. The improvement in the retrieved emissivity should translate into an improvement in the retrieved skin temperature. This is indeed the case as can be seen from Figure 11. The TPW retrieval error is also presented.

Table 4. RMS difference; A: Between averaged emissivity and true B: Between retrieved and true emissivity using a climatological background mean and covariance C: Between retrieved and true emissivity using a background mean and covariance derived from previous 16 runs. For 1176 NOAA-88 profiles clear sky.

Channel	A	B	C
19V	0.0114	0.0121	0.0113
19H	0.0111	0.0119	0.0111
22V	0.0132	0.0139	0.0132
37V	0.0117	0.0125	0.0116
37H	0.0115	0.0125	0.0115
85V	0.0174	0.0184	0.0174
85H	0.0195	0.0206	0.0195

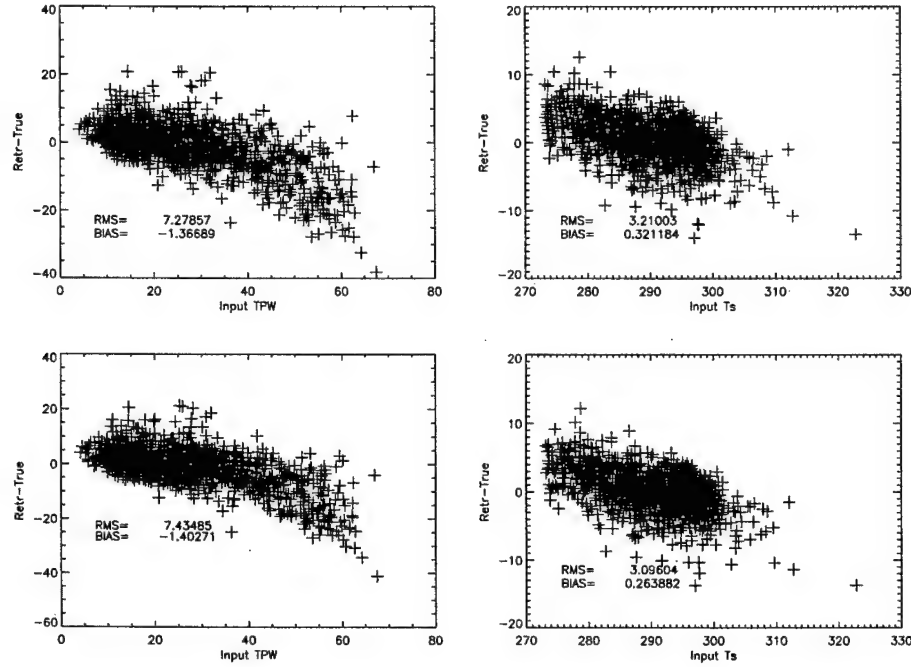


Figure 11. Difference between retrieved and true TPW and skin temperature verse input values. Upper panel: background and covariance generated from Prigent data set. Lower panel: background and covariance generated from retrievals.

Next, we did the same runs but for cloudy conditions. For each point and run we put in a cloud with random height and amount (Figure 12). Table 5 shows the RMS difference between true averaged retrieved and retrieved for this case. Figure 13 shows the retrievals using and not using the background mean and covariance determined from the previous sixteen runs. There is a large improvement in the skin temperature retrieval although no improvement over the clear sky case.

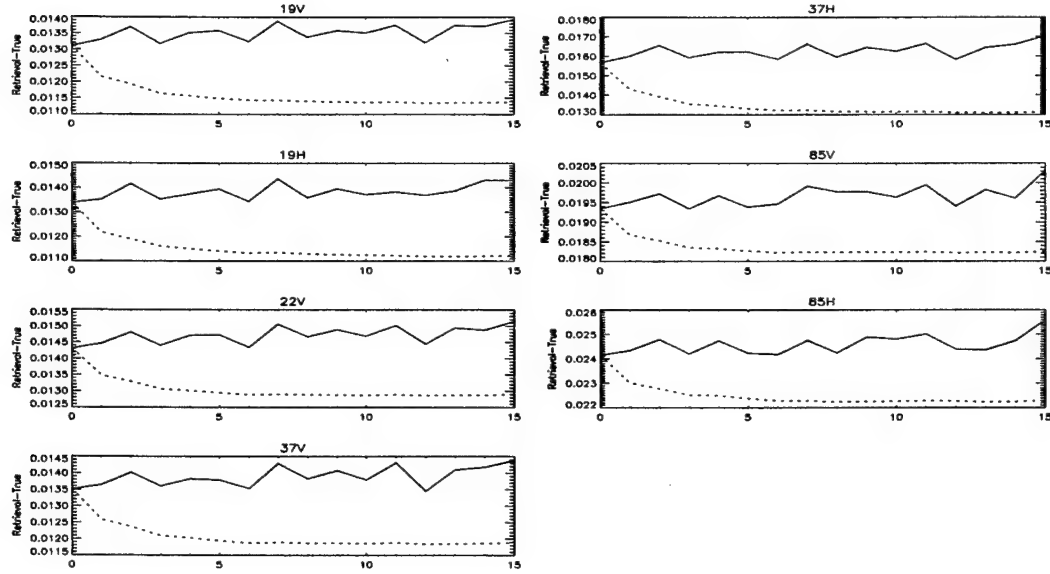


Figure 12. RMS difference between input and averaged (dotted line) and instantaneous (solid line) for all seven channels and sixteen runs. Random cloud height and amount with varying noise.

Table 5. Same as Table 4 except cloudy conditions.

Channel	A	B	C
19V	0.0114	0.0137	0.0112
19H	0.0112	0.0143	0.0114
22V	0.0128	0.0149	0.0127
37V	0.0118	0.0142	0.0118
37H	0.0113	0.0171	0.0132
85V	0.0182	0.0201	0.0184
85H	0.0222	0.0254	0.0224

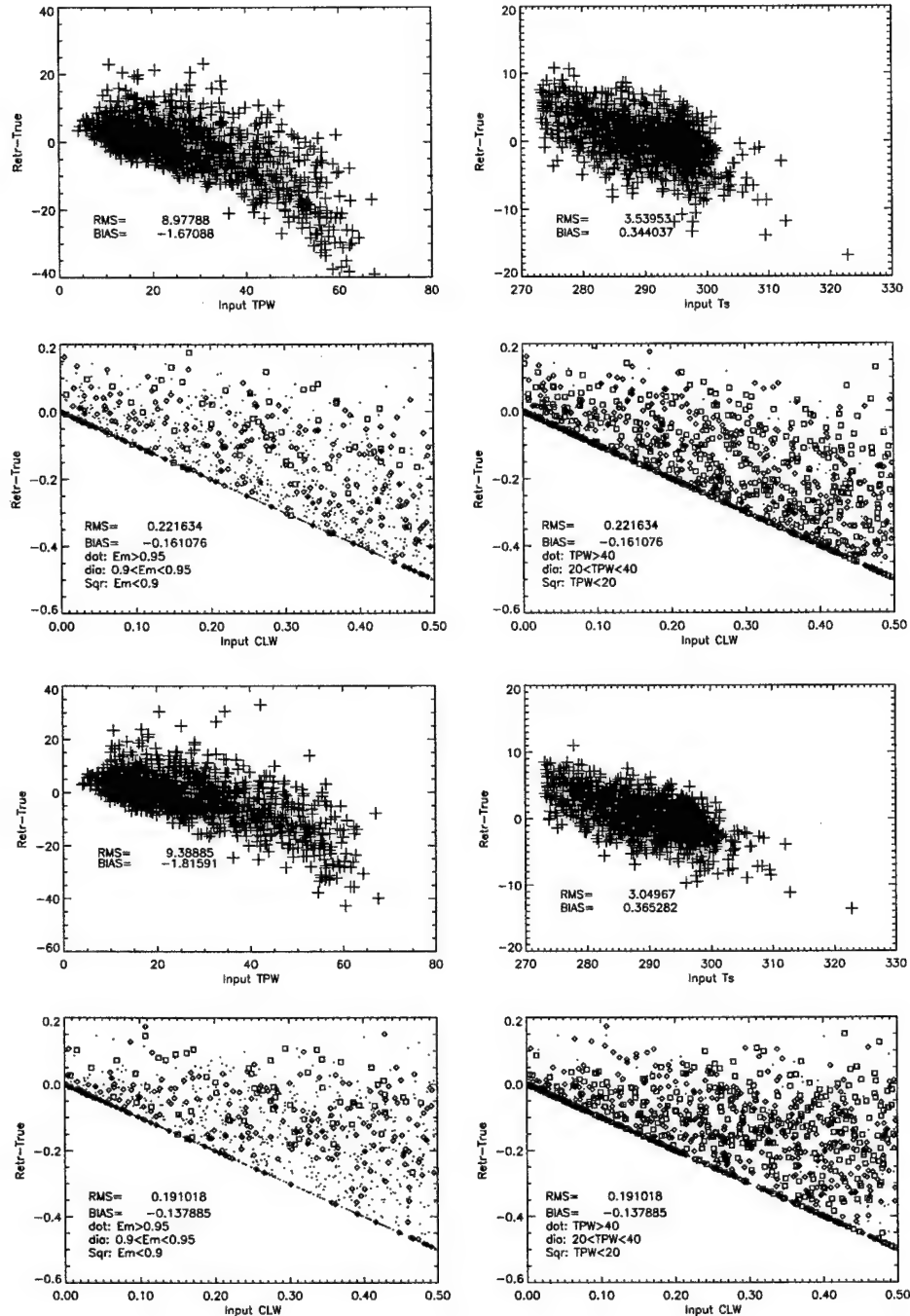


Figure 13. Difference between retrieved and true TPW, skin temperature and CLW verse input values. Upper panels: background and covariance generated from Prigent data set. Lower panels: background and covariance generated from retrievals. The CLW retrievals are stratified in both 19V emissivity range and TPW range.

In the above runs the atmospheric profiles were held constant for each NOAA-88 point. Only the instrument noise and cloud properties were varies. To look at a more realistic situation we did the same exercise on 176 NWP grid points. The data is from 10/1-10/8 in 1995 for 0Z and 12Z each day. Thus, we have sixteen separate profiles for each grid point from the 0Z 10/9 field. Figure 14 shows the RMS difference between input and averaged retrieved and instantaneous retrieved for the sixteen times. As with the cases above the averaged have a lower RMS than the instantaneous. Next, the retrievals were done using and not using the background mean and covariance determined from the previous sixteen runs.

Table 6 lists the RMS difference between the input and retrieved. Figure 15 shows the retrieval error for skin temperature and TPW. There is an improvement in the retrieval of both parameters when the time averaged background mean and covariance is used. A comparison of monthly mean emissivity at 19H GHz from the UR retrieved and Prigent database is shown in Figure 16. This figure shows that the means are in good agreement both spatially and in terms of intensity.

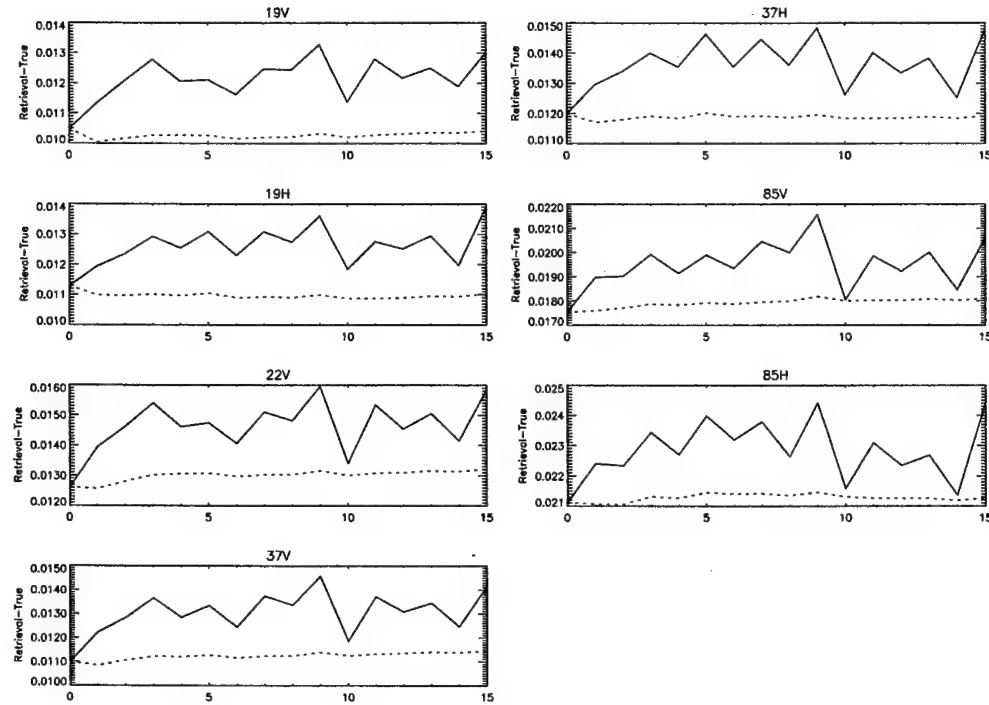


Figure 14. RMS difference between input and averaged(dotted line) and instantaneous(solid line) for all seven channels and sixteen runs. NWP fields

Table 6. Same as **Table 4** except 176 NWP grid points.

Channel	A	B	C
19V	0.0104	0.0128	0.0107
19H	0.0110	0.0132	0.0109
22V	0.0132	0.0151	0.0135
37V	0.0114	0.0134	0.0115
37H	0.0119	0.0137	0.0117
85V	0.0180	0.0196	0.0181
85H	0.0212	0.0225	0.0210

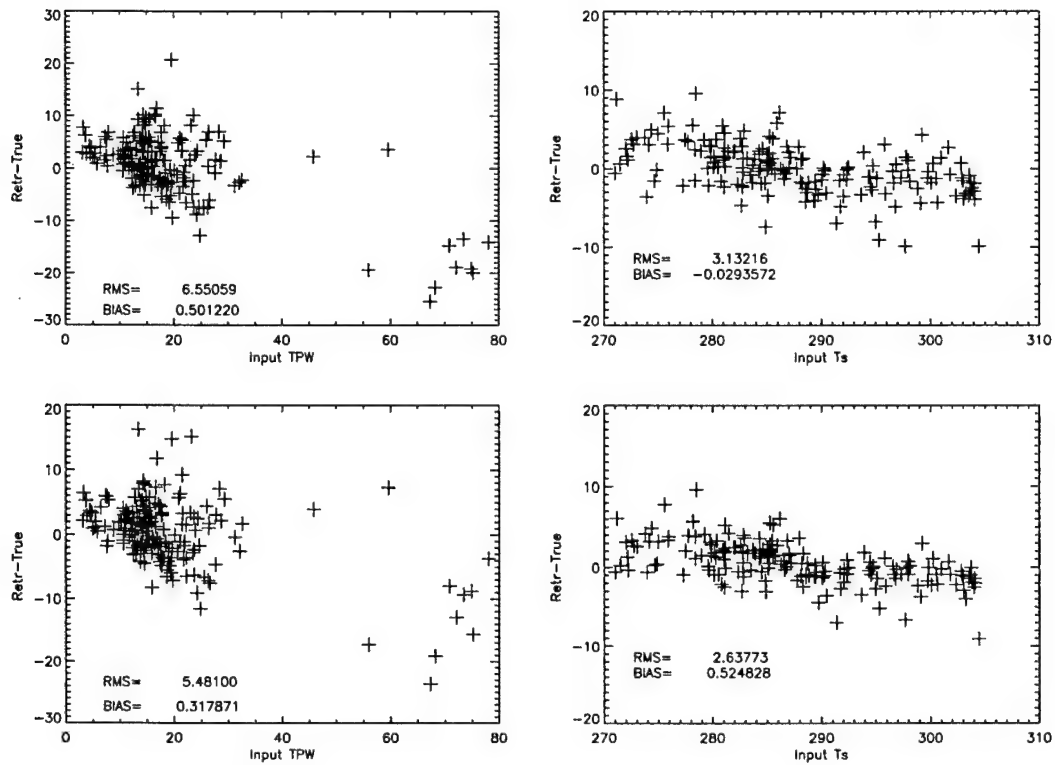


Figure 15. Difference between retrieved and true TPW and skin temperature verse input values. Upper panel: background and covariance generated from Prigent data set. Lower panel: background and covariance generated from retrievals.

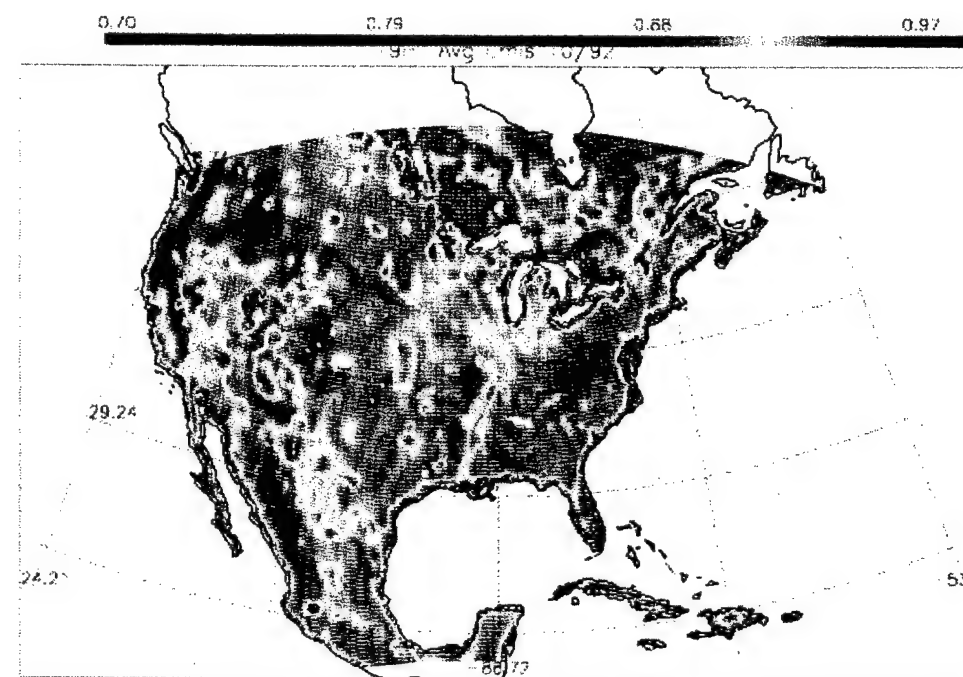
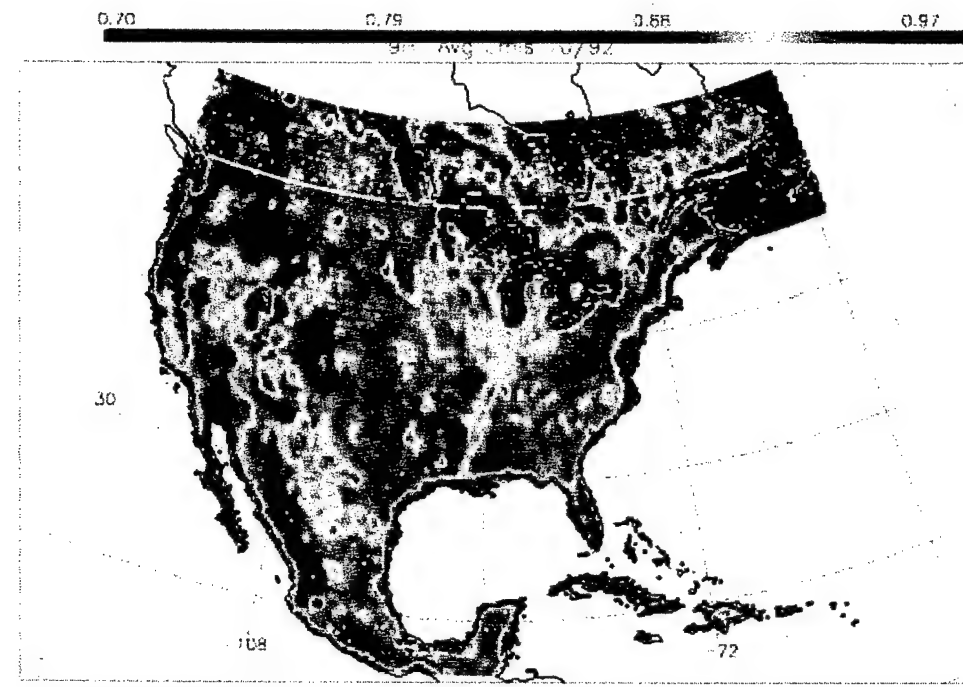


Figure 16. 19H emissivity monthly mean from UR retrieved (top) and Prigent database (bottom).

Surface Air Temperature Retrieval using SSM/I

Retrievals of the surface skin temperature using SSM/I were compared to the 2m temperature reported by NWS shelter boxes for a six day period in October 1995. The comparison shows that the RMS difference between the retrieved surface skin temperature and the shelter box 2 m air temperature to be about 3 K, with a bias of -0.1 K (see Figure 17). Comparison of these same retrievals with those retrieved using the McFarland regression type algorithm show fairly good agreement over a broad range of temperature, but significant discrepancies exist at both high and low temperatures (see Figure 18).

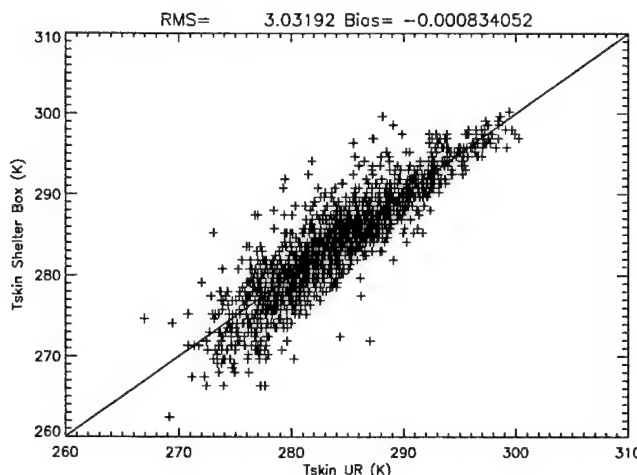


Figure 17. Comparison of retrieved surface skin temperature with shelter box 2 m air temperature.

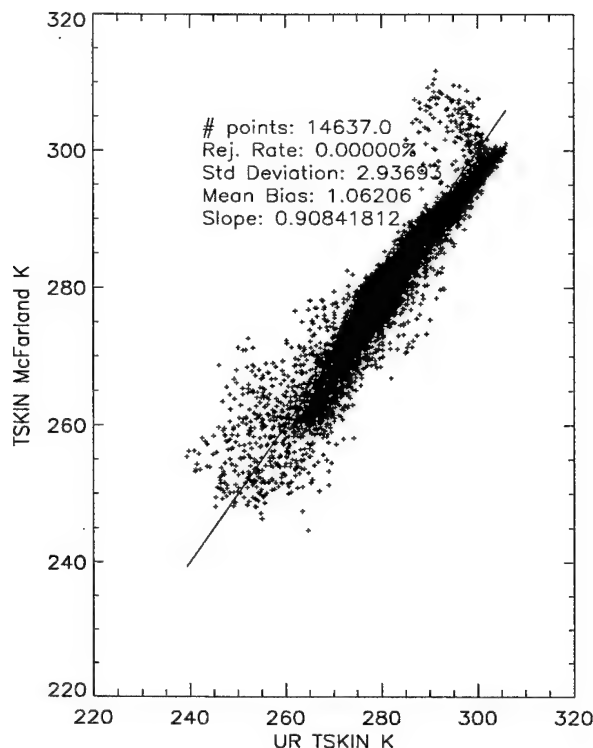


Figure 18. Comparison of UR and McFarland retrievals.

Temperature Profile Retrieval over Land/Snow/Ice using AMSU

Recently the Advanced Microwave Sounding Unit (AMSU) sensor became operational on the NOAA-15 polar orbiting satellite. This sensor consists of AMSU-A, a 15 channel temperature sounder, and AMSU-B, a five channel moisture sounder (see Table 7). Due to calibration problems with AMSU-B, only AMSU-A observations are used for the work presented here. Atmospheric profile retrievals over land surfaces using microwave observations are particularly challenging due to the natural variability of the surface emissivity at microwave frequencies. Comparisons of retrieved atmospheric profiles with NCEP/NCAR Reanalysis data and radiosonde profiles show favorable agreement.

The AMSU data were obtained from the NOAA Satellite Active Archive as level 1b data and were limb corrected over ocean and land using the coefficients given by Chalfant at NOAA NESDIS FPDT (personal communication). This correction reduces the scan line dependent errors found in the native data set and makes the limb correction. The native data were found to largely unusable without this correction.

Temperature profiles were retrieved from the AMSU-A data, globally, during the month of February 1999. Comparisons of retrieved temperature profiles with radiosonde observations over the United States indicate that the retrieval uncertainty (RMS), including temporal, spatial, and radiosonde measurement error, is about 3-4 K near the surface. Throughout the depth of the troposphere it is at or below 2 K, increasing to 3 to 4 K at the tropopause. Retrieval errors using simulated data indicate that the RMS error should be approximately 2.5 K near the surface, 1.5 K in the mid-troposphere, and 2 K at the tropopause. The additional error incurred in the radiosonde comparison of about 0.5 to 1.5 K could be from spatial (volume-point sampling) and temporal differences and/or errors from the limb correction. Since radiosonde measurement spacing is insufficient in time and space, it is difficult to account for these errors quantitatively. The retrieved surface temperature and precipitable water are shown along with the surface map in Figure 20. The retrieved precipitable water field clearly depicts the analyzed surface front. A comparison of the retrieved temperature at 700 mb with NCEP/NCAR Reanalysis data for February 11, 1999 is shown in Figure 21. The retrieved emissivity for 23 and 89 GHz is shown for February 4, 1999, in Figure 22. Regions where emissivities are high at 23 GHz and low at 89 GHz probably have snow or ice surfaces. Regions where emissivities at both 23 and 89 GHz are low probably have very wet soil or standing water. The corresponding temperature retrievals at 700 mb along with the NCEP and radiosonde values are shown in Figure 23. The

temperature field further north is shown in Figure 24. The retrieval agrees well with the reanalysis and the sondes all the way up to and including Greenland.

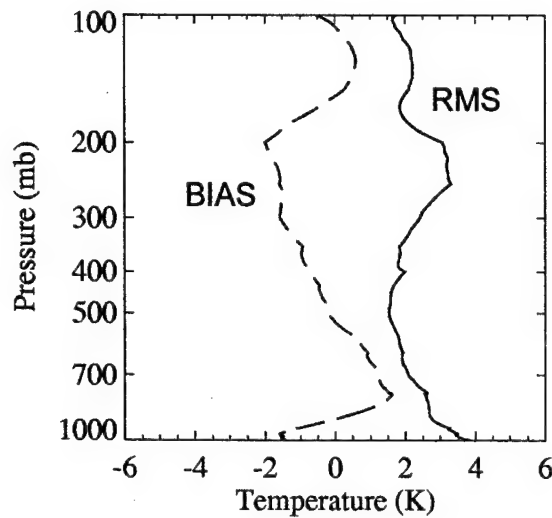


Figure 19. RMS and bias for retrieval - radiosonde comparison for both ascending and descending passes over the USA during February 1999

Table 7. Advanced Microwave Sounding Unit (AMSU) channel specifications. AMSU-A: Channels 1-15, AMSU-B: Channels 16-20.

Channel Number	Central Frequency (GHz)	Side Band (GHz)	Bandwidth (MHz)	Primary Use
1	23.800	0.0	270	TPW
2	31.400	0.0	180	CLW
3	50.300	0.0	180	Temperature
4	52.800	0.0	400	Temperature
5	53.596	± 0.115	170	Temperature
6	54.400	0.0	400	Temperature
7	54.940	0.0	400	Temperature
8	55.500	0.0	330	Temperature
9	57.290	0.0	330	Temperature
10	57.290	0.217	78	Temperature
11	57.290	$\pm 0.322 \pm 0.048$	36	Temperature
12	57.290	$\pm 0.322 \pm 0.022$	16	Temperature
13	57.290	$\pm 0.322 \pm 0.010$	8	Temperature
14	57.290	$\pm 0.322 \pm 0.0045$	3	Temperature
15	89.000	0.0	6000	CLW
16	89.000	± 0.9	1000	CLW
17	150.000	± 0.9	1000	Water vapor
18	183.310	± 1.0	500	Water vapor
19	183.310	± 3.0	1000	Water vapor
20	183.310	± 7.0	2000	Water vapor

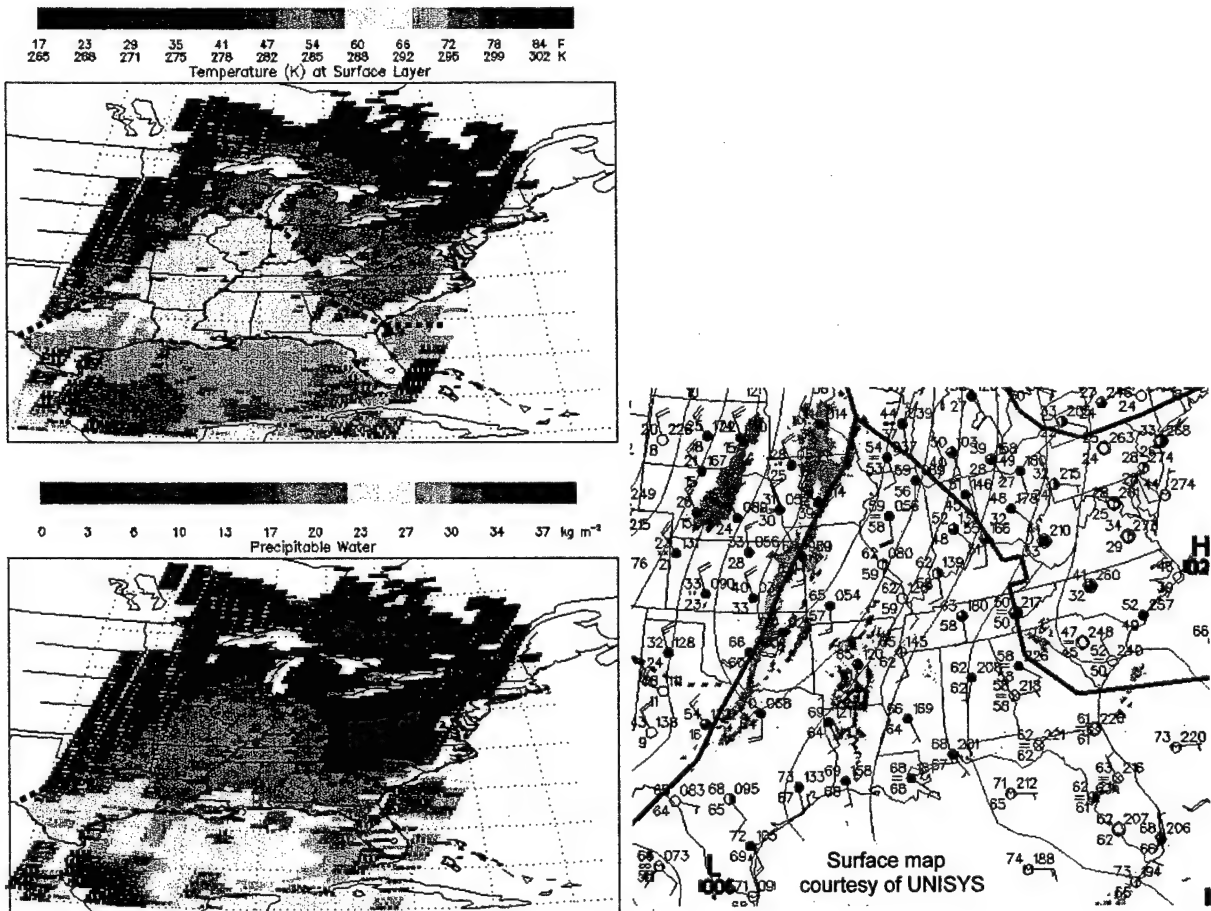


Figure 20. Surface Temperature and Precipitable water retrieval for February 11, 1999. Dotted line represent surface front as depicted on surface map.

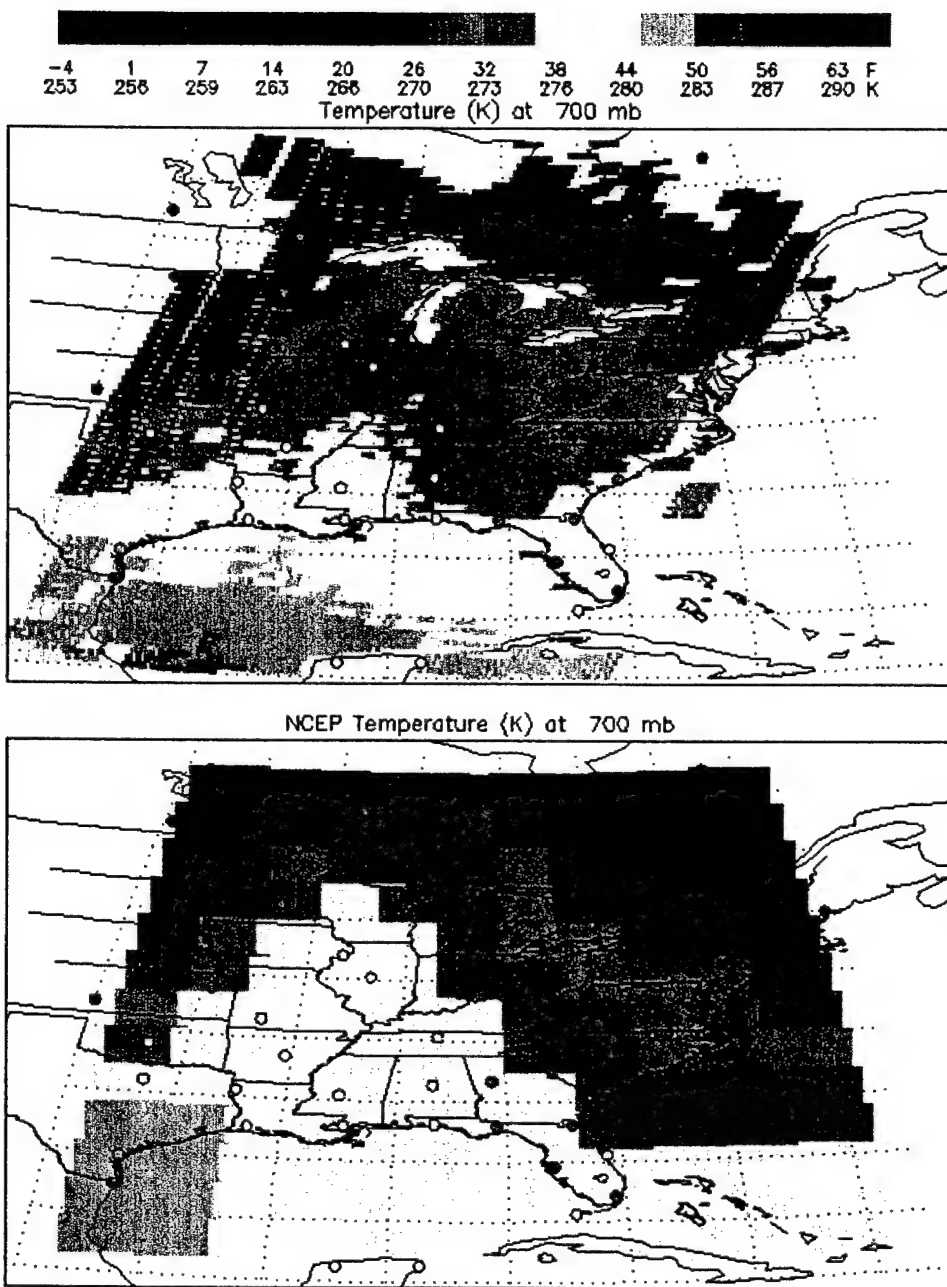


Figure 21. Retrieved and NCEP reanalysis temperature at 700 mb. Circles indicate radiosonde-measured temperature at 700 mb.

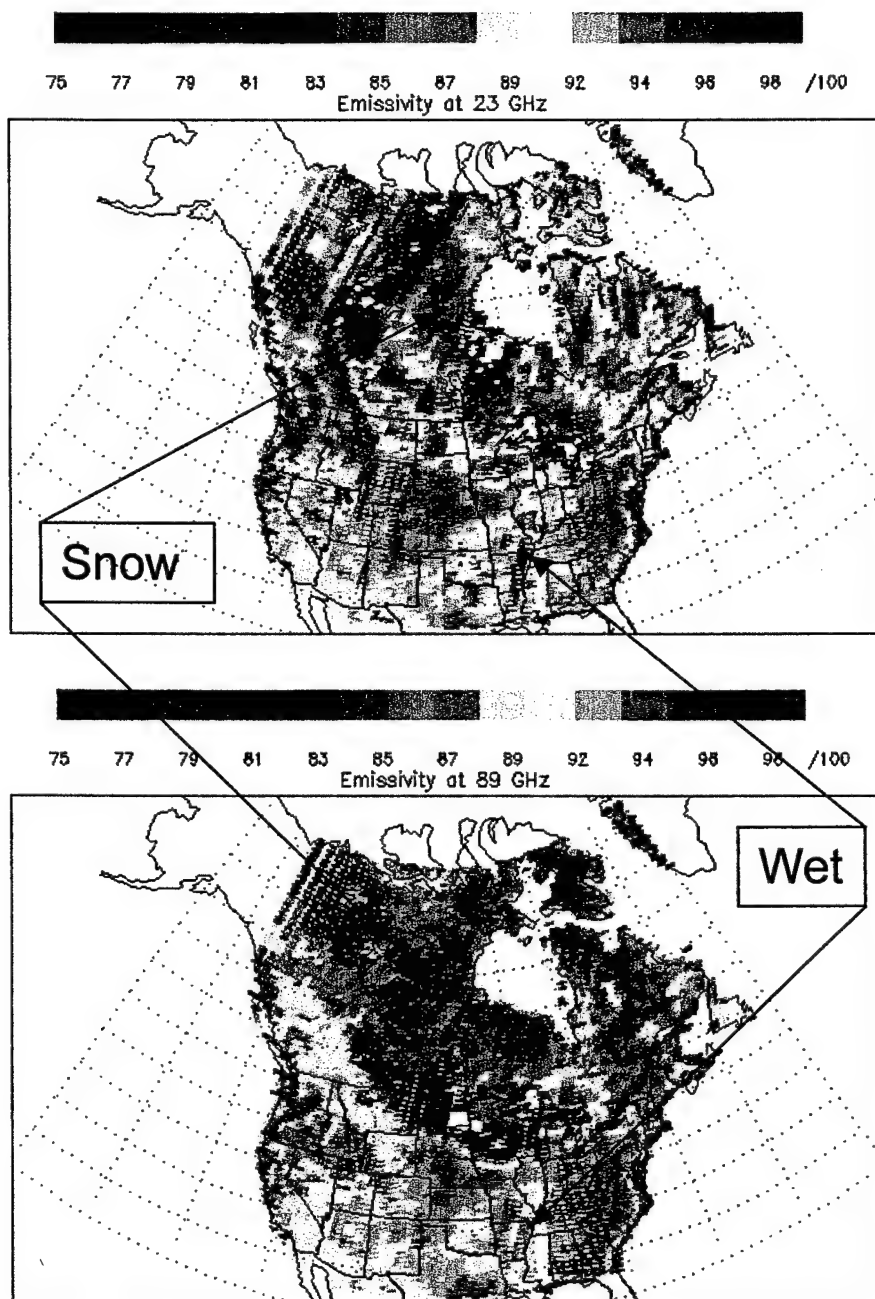


Figure 22. Retrieved surface emissivity at 23 and 89 GHz, February 4, 1999

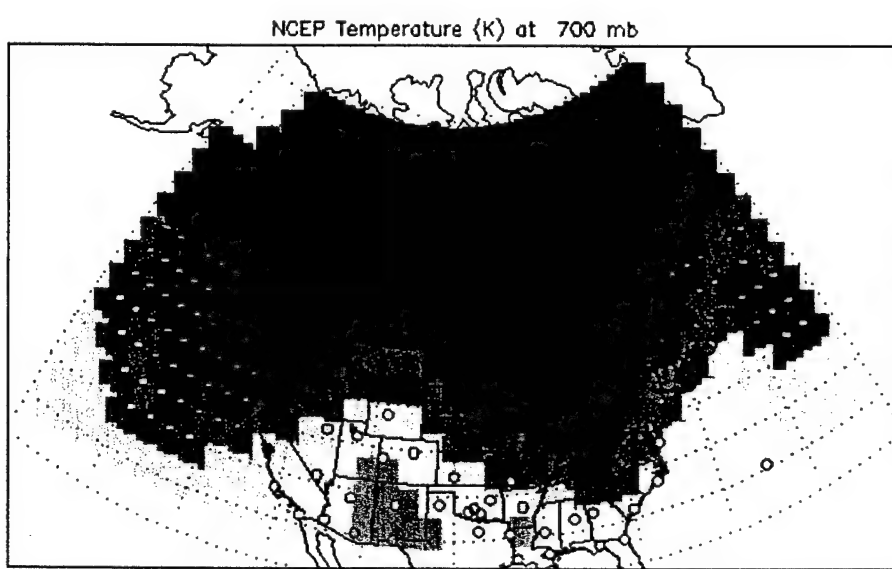
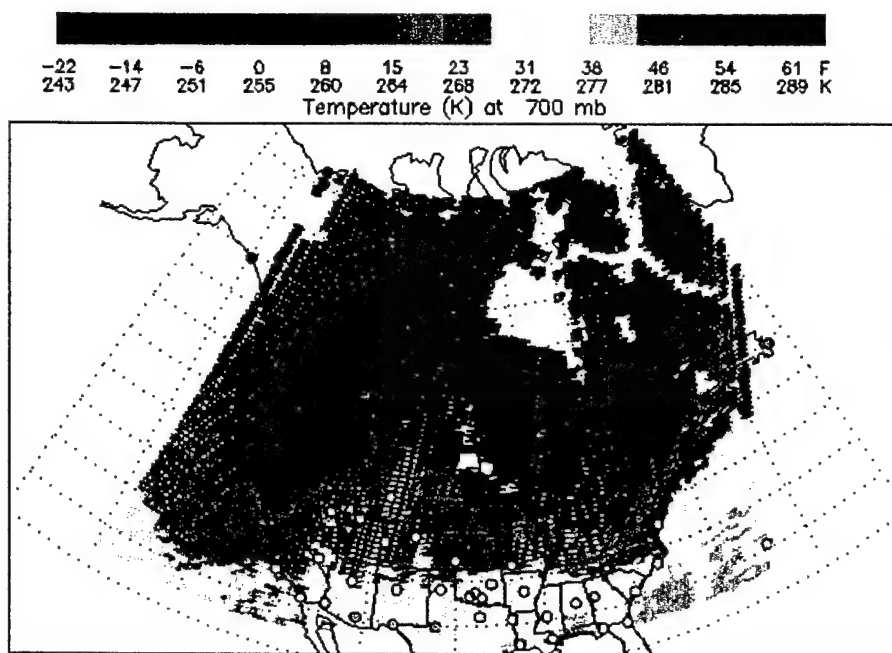


Figure 23. Retrieved and NCEP reanalysis temperature at 700 mb on February 4, 1999. Circles indicate radiosonde-measured temperature at 700 mb.

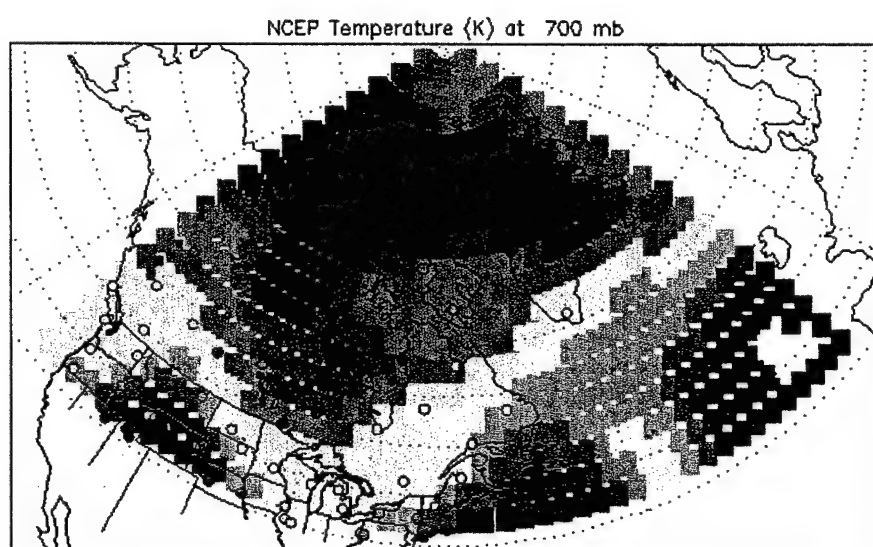
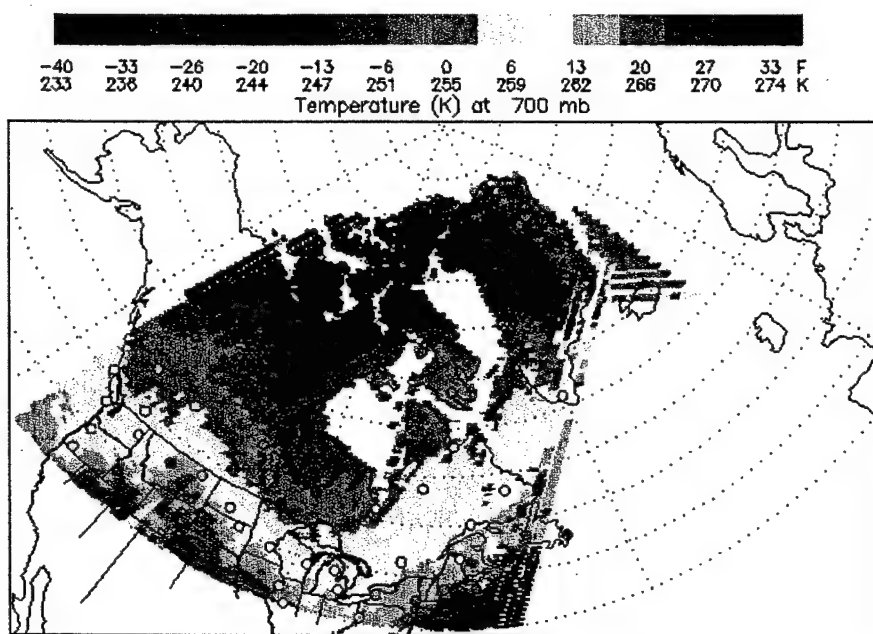


Figure 24. Retrieved and NCEP reanalysis temperature at 700 mb on February 4, 1999. Circles indicate radiosonde-measured temperature at 700 mb.

Conclusions

This report has described the advancements made in the application of the UR algorithm. Studies included further investigation in the retrieval of surface emissivity, temperature, moisture, and clouds over land surfaces. Additionally, a cloud modeling error analysis has been completed. New work included the identification of clouds using microwave-based retrievals along with IR observations and the use of AMSU observations to retrieve temperature over snow and ice surfaces.

Retrievals of land surface emissivity simultaneously with temperature, moisture, and cloud was shown to agree with that of Prigent in a monthly mean sense. The retrieval of the emissivity is sufficiently accurate to allow for the retrieval of other parameters like temperature and moisture. However, comparisons with radiosonde measurements near the surface indicate that the retrieval error is larger near the surface with emissivity error likely contributing to that increased difference. Characterization of the surface emissivity of snow and ice surfaces from the Prigent dataset is sufficient for the UR algorithm to retrieve reasonable temperature and moisture profiles over the snow and ice as compared to radiosonde measurements. Using simulated clear sky infrared radiances with the retrieved temperature and moisture profiles from the DMSP suite aboard F11 as input to the forward model, we were able to consistently predict the observed visible albedo given the observed infrared measurements. Although this study was preliminary and small-scale, the accurate prediction of the visible albedo and hence the presence of cloud would very useful for aviation safety and tactical aides. Further work demonstrating that these methods work on a global scale is necessary. Additional work is also necessary to validate the retrievals over land to establish a thorough analysis of the error budget.

References

Alishouse, J.C., S.A. Snyder, J. Vongsathorn, and R.R. Ferraro, 1990: Determination of oceanic total precipitable water from the SSM/I. *IEEE Trans. on Geosci. and Remote Sensing*, **28**, 811-816.

Eyre, J. R., 1989: Inversion of cloudy satellite sounding radiances by nonlinear optimal estimation: application to TOVS data, *Q. J. R. Meteorol. Soc.*, **115**, 1027-1037.

Isaacs, R.G., 1989: A unified retrieval methodology for the DMSP meteorological sensors. in *RSRM '87: Advances in Remote Sensing Retrieval Methods*. Deepak Publishing. pp. 203-213.

Inoue, T., 1984: On the temperature and effective emissivity determination of semi-transparent cirrus clouds by bi-spectral measurements in the 10 μm window region. *Journal of the Meteorological Society of Japan.*, **63**, 88-98.

McFarland, M.J., R.L. Miller, and C.M.U. Neale, 1990: Land surface temperature derived from the SSM/I passive microwave brightness temperatures. *TGARS.*, **28**, 839-845.

Moncet, J.L., R.G. Isaacs, and J. D. Hegarty, 1996: Unified retrieval of atmospheric temperature, water substance, and surface properties from the combined DMSP sensor suite. PL-TR-96-2067 Final Report. Phillips Laboratory, Directorate of Geophysics, AFMC, Hanscom AFB, MA 01731-5000.

Poe, G.A., 1990: Optimum interpolation of imaging microwave radiometer data. *TGARS.*, **28**, 800-810.

Prigent, C., W. B. Rossow, and E. Matthews, 1997: Microwave land emissivities estimated from SSM/I observations, *J. Geophys. Res.*, **102**, 21867-21890.

Rodgers, C. D., 1976: Retrieval of atmospheric temperature and composition from remote measurements of thermal radiance, *Rev. Geophys.*, **14**, 609-624.

Wu, M.C., 1987: A method for remote sensing the emissivity, fractional cloud cover and cloud top temperature of high level, thin clouds, *Journal of Climate and Applied Meteorology.*, **26**, 225-233.

APPENDIX

1 Forward Modeling

1.1 Radiative Transfer Equations

1.1.1 Microwave

The radiative transfer equation (RTE) used in the microwave region treats the atmosphere as a homogeneous, plane-parallel, non-scattering medium. The brightness temperature, R_ν , at a given frequency ν is computed using the Rayleigh-Jeans approximation as:

$$R_\nu \equiv \varepsilon_\nu \Theta_s T_{s,\nu} + \int_{p_s}^0 \Theta(p) \frac{\partial T_\nu(p, \theta_u)}{\partial p} dp + (1 - \varepsilon_\nu) T_{s,\nu} \left[\int_0^{p_s} \Theta(p) \frac{\partial T_\nu^*(p, \theta_d)}{\partial p} dp + T_\nu^*(0, \theta_d) \Theta_c \right] \quad (1)$$

where $\Theta(p)$ is the atmospheric temperature at pressure p , $T_\nu(p, \theta_u)$ is the total transmittance due to molecular species and cloud liquid water from pressure p to space at the satellite viewing angle θ_u , $T_\nu^*(p, \theta_d)$ is the transmittance from surface to pressure p at computational angle θ_d , ε_ν is the surface emissivity, and Θ_c is the cosmic radiation term ($\Theta_c = 2.73$ K). In the microwave, over both land and ocean, the surface is treated as specularly reflective, i.e. $\theta_d = \theta_u$.

1.1.2 Infrared

The general form of the RTE in the infrared can be written as:

$$R_\nu = \varepsilon_\nu B_\nu(\Theta_s) T_s + \int_{p_s}^0 B_\nu(\Theta(p)) \frac{dT_\nu(p, \theta_u)}{dp} dp + 2 T_s \int_0^{\frac{\pi}{2}} \rho_\nu(\theta_{obs}, \theta) \left[\int_0^{p_s} B_\nu(\Theta(p)) \frac{dT_\nu^*(p, \theta)}{dp} dp \right] \sin \theta \cos \theta d\theta + \rho_\nu T_s T(p_s, \theta_{sun}) F_{0,\nu} \cos(\theta_{sun}) \quad (2)$$

where $B_\nu(\Theta(p))$ is the Planck function emission, $F_{0,\nu}$ is the intensity of the solar radiation, θ_{sun} is the local solar zenith angle and ρ_ν is the bi-directional surface solar reflectance. The third term in Equation (3) represents the contribution of the reflected downwelling thermal radiation to the observed radiance.

A proper consideration of the anisotropy in the downwelling thermal radiance field and surface reflectance properties would require replacing the flux integral by a discrete summation over a pre-determined set of quadrature angles.

In practice, because of the non-homogenous nature of the atmosphere and the fact that bi-directional reflectance (BRDF) properties of natural land surfaces are poorly known, the usefulness of such a level of sophistication in the context of the 1-D retrieval problem is arguable. The following form of RTE is used to address the case of specular and Lambertian surfaces:

$$R_\nu \cong \varepsilon_\nu B_\nu(\Theta_s) T_s + \int_{p_s}^0 B_\nu(\Theta(p)) \frac{dT_\nu(p, \theta_u)}{dp} dp + (1 - \varepsilon_\nu) T_s \int_0^{p_s} B_\nu(\Theta(p)) \frac{dT_\nu^*(p, \theta_d)}{dp} dp + \rho_\nu T_N T F_{0,\nu} \cos(\theta_{sun}) \quad (3)$$

where $\theta_d = \theta_u$ for specular surfaces and $\theta_d \sim 53^\circ$ over Lambertian surfaces. The form of treatment adopted in the Lambertian case results from the use of a single quadrature angle ("diffusivity" angle) to approximate the downward thermal flux.

The present model is valid over ocean where the specular assumption is a reasonable approximation and densely vegetated land surfaces, which BRDF are nearly isotropic. More complex land surface types will be considered in the next phase of this project. In particular, land surface types such as sand, snow, senescent vegetation, as well as inhomogeneous pixels (e.g. mixture of land and water bodies) may display highly non-Lambertian characteristics [Snyder and Wan, 1998]. As a future enhancement to the present algorithm capabilities, we are considering performing a separate retrieval of the thermal reflectivity, over land and coastal regions. Appropriate constraints will be used to tie the spectral thermal reflectivity to the emissivity as a function of geographical location, season, and/or surface/vegetation type.

1.2 Overview of the OSS Method

The Optimal Spectral Sampling (OSS) method is a generalized formulation for the forward radiative transfer problem that is applicable for any type of instrument configuration from the microwave through the ultraviolet regions of the spectrum. With OSS, the radiative transfer is computed at selected wavenumber locations within the spectral interval spanned by the instrument function and the results are combined linearly in such a way as

to accurately represent the radiance for each instrument channel. To accomplish this, the convolution of the monochromatic space-to-level transmittance with the instrument response function (IRF) is approximated as a sum of monochromatic transmittances computed at selected spectral points within the domain spanned by the IRF:

$$T_{\Delta\nu} = \int_{\Delta\nu} \phi_{\nu} T_{\nu} d\nu = \sum_i w_i T_{\nu_i} \quad (4)$$

where ϕ_{ν} represents an instrument function which is assumed to vanish to zero outside the interval $\Delta\nu$ and where $\nu_i \in \Delta\nu$. The optimal selection of the ν_i 's and the computation of the weights, w_i , is performed off-line by comparing the radiances derived using the approximate OSS formulation to those obtained with a reference line-by-line (LBL) model. The optimization procedure minimizes the RMS difference between the "exact" and approximate radiances calculated for an ensemble of globally representative atmospheric profiles over the full range of satellite viewing angles. The following constraints are applied in order to ensure a physical solution:

$$w_i > 0 \quad \text{and} \quad \sum_i w_i = 1 \quad (5)$$

The numerical accuracy of the OSS model is pre-selectable and determines the number of points used in Equation (12) to approximate the exact radiances in each channel. The line-by-line radiative transfer model chosen as a reference in the infrared is the LBLRTM model [Clough *et al.*, 1992]. LBLRTM is originally based on FASCODE and has been extensively validated against atmospheric measurements [Snell *et al.*, 1992]. Figure 1 and Figure 2 compare the brightness temperatures in AMSU (1 to 15) and MHS (16 to 20) channels obtained with the OSS approach and the commonly used "central frequency" approximation with the "exact" calculations from Rosenkranz's model. The RMS differences between the models do not include errors due to optical depth interpolation. These errors can be made arbitrarily small by increasing the number of entries in the optical depth look-up tables.

Table 1 shows the number of OSS points used in the modeling of AMSU radiances. The average RMS error is 0.0135 and the total number of OSS frequencies is 48. Like in the infrared the nominal accuracy of this selection is 0.025 K.

Table 1: Number of Spectral Points Selected in the MW.

Channel Number	Center Frequency (GHz)	Number of OSS Frequencies	RMS
1	23.800	1	0.0009
2	31.400	1	0.0019
3	50.300	1	0.0060
4	52.800	3	0.0042
5	53.596	3	0.0049
6	54.400	3	0.0016
7	54.940	3	0.0263
8	55.500	3	0.0168
9	57.290	1	0.0188
10	57.290	3	0.0221
11	57.290	3	0.0310
12	57.290	3	0.0290
13	57.290	3	0.0258
14	57.290	3	0.0378
15	89.000	2	0.0006
16	89.000	2	0.0005
17	150.000	2	0.0025
18	183.310	2	0.0164
19	183.310	3	0.0066
20	183.310	3	0.0166

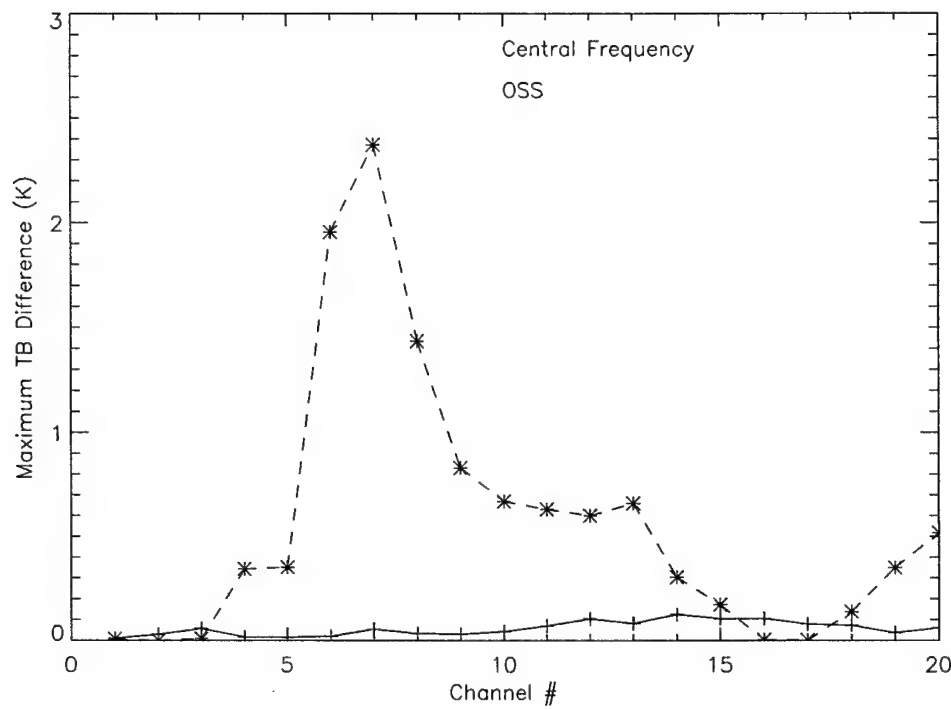


Figure 1: Comparison OSS/Central Frequency (Maximum Differences).

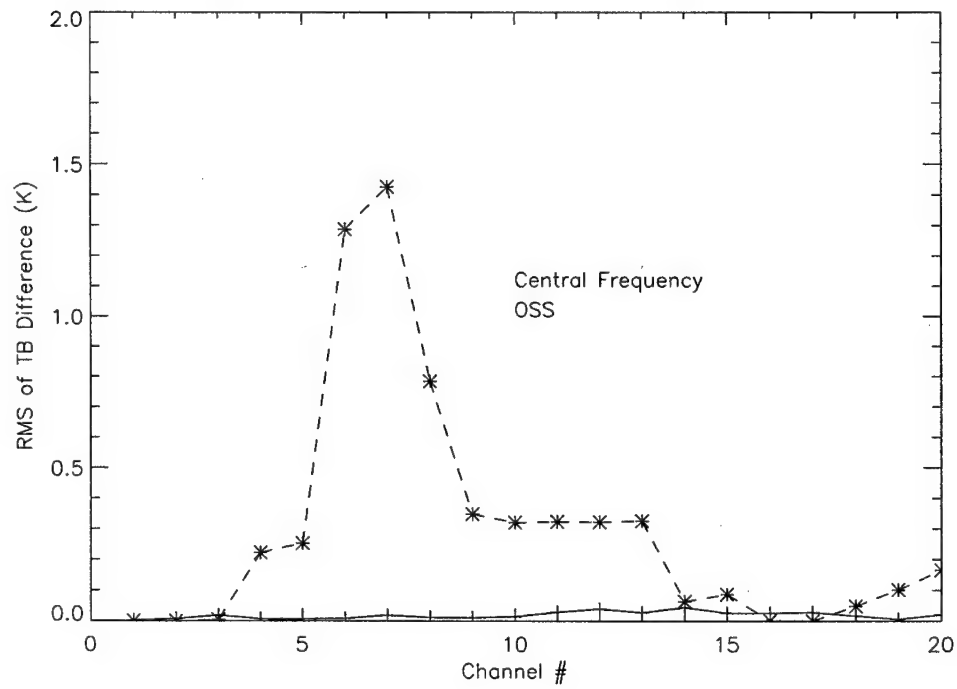


Figure 2: Comparison OSS/Central Frequency (RMS).

1.3 Transmittance Model

To compute transmittance, the OSS model makes use of pre-stored monochromatic layer optical depths for the relevant atmospheric gases at the selected wavenumber locations. The gases are split into two groups, those that have a fixed molecular amount and those that are variable. Because a single optical depth represents the fixed gases this grouping reduces the storage requirements for the optical depth tables. For each species, the optical depths are stored at a set of temperatures for each pressure layer used in the discrete radiative transfer model. For each layer this temperature range spans the temperatures expected for that layer based on the profiles in the TIGR [Chedin *et al.*, 1985] and NOAA-88 atmospheric profile databases. This temperature domain is sampled uniformly and the optical depths are stored at 10 temperatures.

The optical depth tables are calculated using the LBLRTM radiative transfer model along with the molecular amounts from the US Standard Atmosphere profile [Anderson *et al.*, 1986]. This model contains state-of-the-art physics, including the latest version of the CKD water vapor continuum [Clough *et al.*, 1989]. Because of the CKD formulation the method of optical depth calculation must be modified slightly for water vapor, since the self-broadened component of the water vapor continuum contains a quadratic dependence on the number density. As such the self-broadened component is separated from the water lines and the foreign-broadened component of the continuum. Absorption coefficients of water vapor lines and foreign broadened continuum are grouped together in one table. A second table contains absorption coefficients of self-broadened water vapor continuum. For a given layer each optical depth is linearly interpolated to the layer temperature. The correct optical depths for the variable species are then obtained by multiplying the temperature-interpolated optical depth by the ratio of the layer amount to the standard amount. This is equivalent to multiplying the species' molecular absorption coefficient by the molecular amount, but reduces numerical accuracy problems encountered because of the many orders of magnitude difference in the value of the absorption coefficient and the molecular amount. Of minimal impact, and thus neglected in the current formulation, is the difference in the self-broadened component of the line shape between the standard density used to compute the stored optical depths and the actual layer density.

Total optical depth is computed for each layer l at nadir as:

$$\begin{aligned}\tau_l^0 = & \tau_{fix}(\bar{p}_l, \theta_l) + (k_{H2O}(\bar{p}_l, \theta_l) + k_{H2O}^{self}(q_{H2O}, \theta_l))\omega_{H2O} + k_{O3}(\bar{p}_l, \theta_l)\omega_{O3} \\ & + \tau_{CH4}(\bar{p}_l, \theta_l) + \tau_{CO}(\bar{p}_l, \theta_l) + \tau_{N2O}(\bar{p}_l, \theta_l)\end{aligned}\quad (6)$$

where τ is the optical depth, κ is the absorption coefficient, ω is the absorber amount, p is the layer pressure and θ is the temperature. The current set of optical depths is stored at each monochromatic spectral point for 39 layers and 10 temperatures. The optical depth tables for the microwave OSS model are structured in much the same way as for the IR, with only slight differences because of the nature of the microwave spectrum. The total optical depth is computed for each layer l at nadir as:

$$\tau_l^0 = \tau_{O2+N2}(\bar{p}_l, \theta_l, \omega_{H2O}) + \tau_{H2O}(\bar{p}_l, \theta_l, \omega_{H2O}) \quad (7)$$

where the variables are defined as in the infrared equation given above. The calculations are done using the Rozenkranz model [Rosenkranz, 1995]. The microwave optical depths are tabulated as a function of both temperature and water vapor. Simulation studies indicated that 20 temperature and water vapor interpolation points are required for accurate OSS representation under a wide variety of atmospheric conditions. Thus for the 20 AMSU microwave channels the optical depth table occupies 5.99 Mbytes of storage space.

1.4 Radiance Calculation

1.4.1 Overview of the Method

Since the OSS method is a monochromatic approach to the radiative transfer, the gradient of the forward model with respect to all relevant atmospheric/surface parameters can be computed efficiently using an analytical scheme. Computation of radiances and derivatives with the OSS method uses a generic recursive scheme developed for the modeling of upward, downward-looking and limb-viewing instruments and used in atmospheric retrievals from CIRRIS [Miller *et al.*, 1999].

Figure 3 defines the numbering conventions for the layered atmosphere. T_l and T_l^* denote the transmittances from space-to-level and surface-to-level l computed along the upward (u) and downward (d) atmospheric paths, defined as:

$$T_l = \exp\left(-\sum_{i=1}^l \tau_i^0 \sec\theta_{obs}\right) \quad (8)$$

and:

$$T_l^* = \exp\left(-\sum_{i=l}^N \tau_{i+1}^0 \sec\theta_d\right) \quad (9)$$

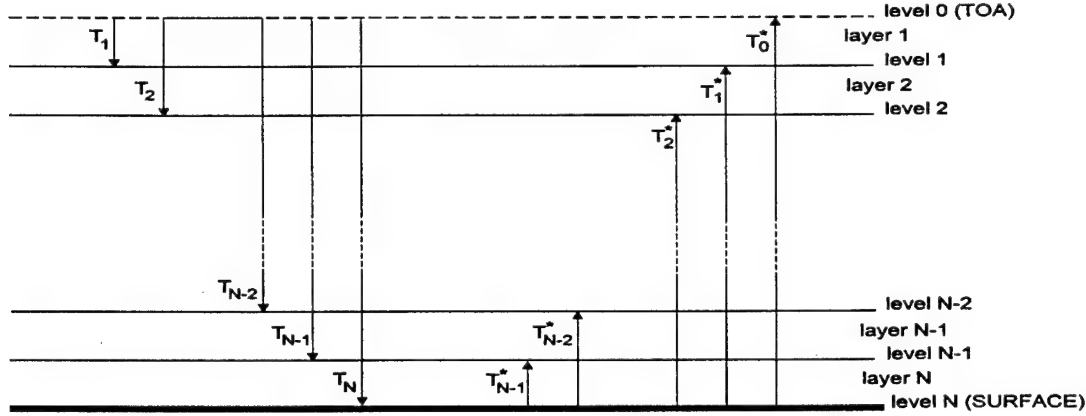


Figure 3: Schematic diagram showing the numbering convention for the atmospheric layers used by OSS, where T refers to transmittances, level 0 represents the top of the atmosphere (TOA) and level N the surface.

Radiance in clear conditions are computed using the following expression derived by discretizing the radiative transfer equation as:

$$R_\nu = \sum_{i=1}^N (T_{\nu,i-1} - T_{\nu,i}) B_{\nu,i}^+ + \varepsilon_{\nu s} T_{\nu,N} B_{\nu,s}^+ + (1 - \varepsilon_{\nu s}) \Gamma_{\nu,N} \sum_{i=1}^N (T_{\nu,i}^* - T_{\nu,i-1}^*) B_{\nu,i}^- \quad (10)$$

where B_ν^\pm represents the upward and downward Planck emission of the layer/surface and $\varepsilon_{\nu s}$ is the surface emissivity. Derivatives of R_ν with respect to constituents concentration or temperature in layer l are obtained by differentiating the previous equation:

$$\begin{aligned} \frac{\partial R}{\partial X_l} = & -\frac{\partial \tau_l^0}{\partial X_l} \left\{ \left[-T_l B_l + \sum_{i=l+1}^N (T_{i-1} - T_i) B_i + T_N \varepsilon_s B_s + (1 - \varepsilon_s) \Gamma_N \sum_{i=1}^N (T_i^* - T_{i-1}^*) B_i \right] \sec \theta_{obs} \right. \\ & \left. + \left[-(1 - \varepsilon_s) \Gamma_N T_{l-1}^* B_l + (1 - \varepsilon_s) \Gamma_N \sum_{i=1}^{l-1} (T_i^* - T_{i-1}^*) B_i \right] \sec \theta_d \right\} \quad (11) \\ & + \frac{\partial B_l^+}{\partial X_l} (T_{l-1} - T_l) + (1 - \varepsilon_s) \Gamma_N \frac{\partial B_l^-}{\partial X_l} (T_l^* - T_{l-1}^*) \end{aligned}$$

or, by introducing the two-path attenuation from level l to space, $T'_l = (1 - \varepsilon_s) \Gamma_N T_l^*$

$$\begin{aligned}
\frac{\partial R}{\partial X_l} = & -\frac{\partial \tau_l}{\partial X_l} \left[-T_l B_l + \sum_{i=l+1}^N (T_{i-1} - T_i) B_i + T_N \epsilon_s B_s + \sum_{i=1}^N (T'_i - T'_{i-1}) B_i \right. \\
& \left. - T'_{l-1} B_l + \sum_{i=1}^{l-1} (T'_i - T'_{i-1}) B_i \right] \\
& + \frac{\partial B_l^+}{\partial X_l} (T_{l-1} - T_l) + \frac{\partial B_l^-}{\partial X_l} (T'_l - T'_{l-1})
\end{aligned} \tag{12}$$

where X_l stands for either θ_l or ω_l^m .

With the exception of the handling of the surface terms, the recursive procedure for the integration of the RTE and calculation of the derivatives over a reflective surface is similar to the one used for limb viewing. This procedure uses the fact that a perturbation in temperature or constituent concentration in any given layer of the atmosphere does not affect the emission in the atmospheric slab comprised between this layer and the observer. Therefore, derivatives can be obtained at low cost if the RTE is integrated by adding layers sequentially in the direction of the observer. The procedure is more apparent by introducing the quantities Σ_l^- and Σ_l^+ defined as the contribution to the observed radiance of the downward emission (reflected at the surface) from the atmosphere above level l and the contribution of the atmosphere below level l plus reflected downward radiation, e.g.:

$$\Sigma_l^- = \sum_{i=1}^l (T'_i - T'_{i-1}) B_i^- \tag{13}$$

and

$$\Sigma_l^+ = \sum_{i=l+1}^N (T_{i-1} - T_i) B_i^+ + \epsilon_s T_N B_s + \sum_{i=1}^N (T'_i - T'_{i-1}) B_i^- \tag{14}$$

where (two-path transmittance):

$$T'_l = (1 - \epsilon_s) T_N T_l^* \tag{15}$$

Using the definitions of the previous equations, one can write:

$$\begin{aligned}
\frac{\partial R}{\partial X_l} = & \left[\frac{\partial R}{\partial X_l} \right]_u + \left[\frac{\partial R}{\partial X_l} \right]_d \\
= & \left[\frac{\partial \tau_l}{\partial X_l} (-\Sigma_{l-1}^- + B_l^- T'_{l-1}) + \frac{\partial B_l^-}{\partial X_l} (T'_{l+1} - T'_l) \right] \\
& + \left[\frac{\partial \tau_l}{\partial X_l} (-\Sigma_l^+ + B_l^+ T_l) + \frac{\partial B_l^+}{\partial X_l} (T_l - T_{l-1}) \right]
\end{aligned} \tag{16}$$

In the current version of the UR algorithm, the following simplifying assumptions are made in the calculation of the derivatives:

- Dependence of atmospheric transmittances on temperature is neglected in the calculations of the derivatives:

$$\partial \tau_l / \partial \Theta_l = 0 \quad (17)$$

- Layer emission is computed as the average Planck emission for the layer:

$$B_l^+ = B_l^- = \bar{B}_l = (B_l^l + B_l^u) / 2 \quad (18)$$

This approximation is adequate as long as layers are not optically thick, e.g. vertical pressure grid is sufficiently fine and no cloud is present. The trade-off between coarseness of the vertical sampling and the use of a more sophisticated approach such as linear-in-tau approximation has not been evaluated yet. It results from this approximation that $\partial B_l / \partial \tau_l = 0$.

1.4.2 Practical Implementation

In a first pass, at any given wavenumber, the algorithm computes the profile of transmittance from space. The recursive procedure for the computation of radiances and analytical derivatives follows directly the last equation written above.

- 1) Initialization: set $\Sigma_0^- = 0$.
- 2) If $(1 - \varepsilon_s)T_N > 10^{-4}$, add layers successively from TOA down to surface.
Update Σ_l^- at each step and compute first part of radiance derivatives.

$$\left[\frac{\partial R}{\partial \tau_l} \right]_d = -\Sigma_{l-1}^- + \bar{B}_l T'_{l-1} \quad (19)$$

and

$$\left[\frac{\partial R}{\partial \Theta_l} \right]_d = \frac{\partial \bar{B}_l}{\partial \Theta_l} (T'_l - T'_{l-1}) \quad (20)$$

$$\Sigma_l^- = \Sigma_{l-1}^- + (T'_l - T'_{l-1}) \bar{B}_l \quad (21)$$

3) Add surface term and compute derivative with respect to surface emissivity and temperature.

$$\frac{\partial R}{\partial \Theta_s} = T_N \epsilon_s \frac{\partial B_s}{\partial \Theta_s} \quad (22)$$

and

$$\frac{\partial R}{\partial \epsilon_s} = T_N B_s - \Sigma_N^- / (1 - \epsilon_s) \quad (23)$$

$$\Sigma_N^+ = \Sigma_N^- + T_N \epsilon_s B_s \quad (24)$$

4) Update Σ_l^+ by adding layers from surface up to TOA and compute second part of derivatives.

$$\frac{\partial R}{\partial \tau_l} = -\Sigma_l^+ + \bar{B}_l T_l + \left[\frac{\partial R}{\partial \tau_l} \right]_d \quad (25)$$

and

$$\frac{\partial R}{\partial \Theta_l} = \frac{\partial \bar{B}_l}{\partial \Theta_l} (T_{l-1} - T_l) + \left[\frac{\partial R}{\partial \Theta_l} \right]_d \quad (26)$$

$$\Sigma_{l-1}^+ = \Sigma_l^+ + (T_{l-1} - T_l) \bar{B}_l \quad (27)$$

5) Set $R_v = \Sigma_0^+$ and compute derivatives with respect to temperature and layer amounts for all molecular species.

$$\frac{\partial R_\nu}{\partial \omega_i^m} = \frac{\partial R_\nu}{\partial \tau_{\nu,l}} \times k_{\nu,l}^m; \quad m=1, \dots, M \quad (28)$$

1.4.3 Microwave Cloud Liquid Water

Cloud optical depths and their derivatives are computed in a subroutine that outputs a profile of cloud optical depth per layer and the derivatives of the layer optical depths with respect to two cloud parameters: total liquid water (Q) and top pressure (p_t). Cloud thickness (Θ) is held constant. Results are produced at the central frequency for each channel.

The layer optical depths are computed as:

$$\tau_{ij} = Q k_{ci}(\bar{T}_j) f \frac{\Delta_j}{\Theta} \quad (29)$$

where τ_{ij} is the optical depth in layer j for frequency index i , k_c is the mass absorption coefficient for liquid water, \bar{T}_j is the average temperature of the cloud within layer j , f is the cloud fraction within the field-of-view.

The cloud proportion that is in layer j is represented by $\frac{\Delta_j}{\Theta}$, where Δ_j is given in Table 2 and cloud base is $p_b = p_t + \Theta$. If the entire cloud depth is within layer j , then $\Delta_j = \Theta$. The mass absorption coefficient is computed from the model of Liebe *et al.* [Liebe *et al.*, 1991], with the alternative, exponential formulation for the primary relaxation frequency dependence on temperature:

$$\gamma_1 = 20.1 \exp(7.88\theta) \quad (30)$$

where:

$$\theta = 1 - \frac{300 \text{ K}}{T} \quad (31)$$

The derivative with respect to total cloud liquid is given as:

$$\frac{\partial \tau_{ij}}{\partial Q} = k_{ci}(\bar{T}_j) f \frac{\Delta_j}{\Theta} \quad (32)$$

As a practical matter, the derivative is computed and then τ is computed as $Q \frac{\partial \tau_{ij}}{\partial Q}$.

The derivative with respect to cloud top is:

$$\frac{\partial \tau_{ij}}{\partial p_t} = Q k_{ci}(\bar{T}_j) f \frac{1}{\Theta} \frac{\partial \Delta_j}{\partial p_t} \quad (33)$$

The formulae for Δ and its derivatives are in Table 2.

Table 2: Δ and its Derivatives.

Condition on layer j	Δ_j	$\frac{\partial \Delta_j}{\partial p_t}$
Outside cloud, except * $p_{j+1} \leq p_t$ or $p_b \leq p_j$	0	0
Contains cloud top $p_j \leq p_t \leq p_{j+1} \leq p_b$	$p_{j+1} - p_t$	-1
Entirely within cloud $p_t \leq p_j \leq p_{j+1} \leq p_b$	$p_{j+1} - p_j$	0
Contains cloud base $p_t \leq p_j \leq p_b \leq p_{j+1}$	$p_b - p_j$	1
Contains entire cloud $p_j \leq p_t \leq p_b \leq p_{j+1}$	Θ	0
* $j+1$ Contains entire cloud $p_{j+1} \leq p_t \leq p_b \leq p_{j+2}$	0	-1
* $j-1$ Contains entire cloud $p_{j-1} \leq p_t \leq p_b \leq p_j$	0	1